REPORT DOCUMENTATION PAGE

AFRL-SR-BL-TR-01-

0254

1. AGENCY USE ONLY *(Leave blank)*	2. REPORT DATE	3. REPORT TYPE AND DATES COVERED
	Apr 4, 2001	Final Technical Report 01 Jul 97 - 30 Jun 00

4. TITLE AND SUBTITLE
Mechanisms and Control of Chaos and Halos in High Power Microwave Tubes

5. FUNDING NUMBERS
F49620-97-1-0480

6. AUTHOR(S)
Dr. Chiping Chen

7. PERFORMING ORGANIZATION NAME(S) AND ADDRESS(ES)
Massachusetts Institute of Technology
Plasma Science & Fusion Center
Cambridge, MA 02139-4307

8. PERFORMING ORGANIZATION REPORT NUMBER

9. SPONSORING/MONITORING AGENCY NAME(S) AND ADDRESS(ES)
AFOSR/NM
801 N. Randolph St, Rm 732
Arlington, VA 22203-1977

10. SPONSORING/MONITORING AGENCY REPORT NUMBER

F49620-97-1-0480

11. SUPPLEMENTARY NOTES

AIR FORCE OFFICE OF SCIENTIFIC RESEARCH (AFOSR)
NOTICE OF TRANSMITTAL DTIC. THIS TECHNICAL REPORT
HAS BEEN REVIEWED AND IS APPROVED FOR PUBLIC RELEASE
LAW AFR 190-12. DISTRIBUTION IS UNLIMITED.

12a. DISTRIBUTION AVAILABILITY STATEMENT
Approved for public release; distribution unlimited.

12b. DISTRIBUTION CODE

13. ABSTRACT *(Maximum 200 words)*

This report summarizes our research carried out under the auspices of the above referenced grant from July 1, 1997 to June 30, 2000. The goal of this research is to investigate chaos, halos and confinement in beam plasmas in regimes relevant to the development of advanced microwave/millimeter wave sources. An important issue in the design of HPM tubes is how to prevent high-intensity relativistic electron beams from forming halos because they cause electron beam losses and subsequent plasma formation, of pulse shortening and of breakdown [1]. Under the auspices of the present grant, investigations have been conducted of the confinement of bunched beams in high-power klystron amplifier.

20010427 108

14. SUBJECT TERMS

15. NUMBER OF PAGES
34

16. PRICE CODE

17. SECURITY CLASSIFICATION OF REPORT	18. SECURITY CLASSIFICATION OF THIS PAGE	19. SECURITY CLASSIFICATION OF ABSTRACT	20. LIMITATION OF ABSTRACT
UNCLASSIFIED	UNCLASSIFIED	UNCLASSIFIED	UL

Final Report
AASERT-97: Mechanisms and Control of
Chaos and Halos in High-Power Microwave Tubes
AFOSR Grants No. F49620-97-1-0480

April 4, 2001

Submitted to:
Dr. Arje Nachman
Program Manager
Air Force Office of Scientific Research
801 North Randolph Street, Room 732
Arlington, VA 22203-1977

Submitted by
Dr. Chiping Chen
Principal Investigator

Final Report
AASERT-97: Mechanisms and Control of Chaos and Halos in High-Power Microwave Tubes
AFOSR Grant No. F49620-97-1-0480

This report summarizes our research carried out under the auspices of the above referenced grant from July 1, 1997 to June 30, 2000. The goal of this research is to investigate chaos, halos and confinement in beam plasmas in regimes relevant to the development of advanced microwave/millimeter wave sources.

An important issue in the design of HPM tubes is how to prevent high-intensity relativistic electron beams from forming halos because they cause electron beam losses and subsequent plasma formation, rf pulse shortening and rf breakdown [1]. Under the auspices of the present grant, investigations have been conducted of the confinement of bunched beams in high-power klystron amplifier.

In particular, we studied the confinement of a highly bunched beam propagating through a perfectly conducting drift tube in a uniform magnetic field based on the Green's function description [2] of space charge. In the analysis [3,4], a highly bunched beam was treated as a periodic array of point charges, while an unbunched beam was considered as a line charge, as illustrated in Fig. 2, where a is the radius of the drift tube and L is the period. In Fig. 2, the point charge represents a bunch in a highly bunched beam. Use was made of eigenfunction expansion to compute the Green's functions for the Poisson equation for both the line charge and the periodic array of point charges [2]. Making use of these Green's functions, we computed the electrostatic potential due to the surface charge on the perfectly conducting drift tube. With a proper choice of the vector potential for the applied uniform magnetic field $B_0 \hat{e}_z$, we derived and analyzed non-relativistic Hamilton's equations of motion for both the line charge and the periodic array of point charges.

It was shown [3,4] that for a charge bunch with canonical angular momentum $P_\theta = 0$, the condition for radial confinement is given by

$$\frac{2\omega_p^2}{\omega_c^2} < \frac{1}{1 + \sum_{n=1}^{\infty} \frac{n\alpha}{I_0(n\alpha)I_1(n\alpha)}}, \qquad (1)$$

where $\alpha = 2\pi a / L$, $I_0(x)$ and $I_1(x)$ are the zeroth- and first-order modified Bessel functions of the first-kind, respectively, $\omega_p^2 = \left(4\pi e^2 / m\right)\left(N_{bunch} / \pi a^2 L\right)$ is the effective plasma frequency squared with N_{bunch} being the number of electrons per bunch, and $\omega_c = eB_0 / mc$ is the nonrelativistic electron cyclotron frequency.
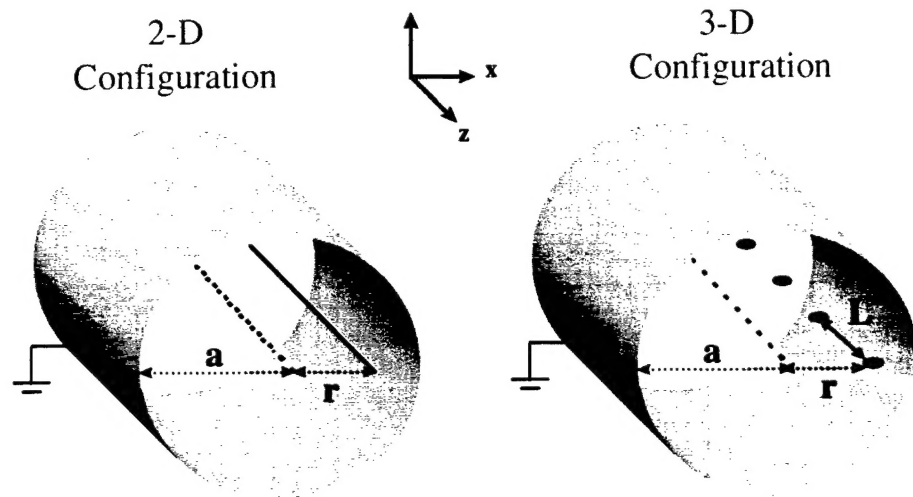
1

2-D Configuration

3-D Configuration

Figure 2. Schematics of a line charge and a periodic array of point charges in a perfectly conducting drift tube.

Figure 3. Plot of the highest value of the effective self-field parameter $2\omega_p^2 / \omega_c^2$ as a function of $\alpha = 2\pi a / L$ for radial confinement of unbunched (2D) and highly bunched (3D) beams.
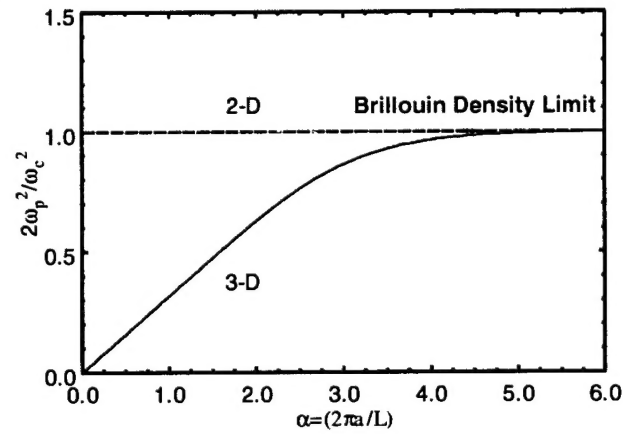
2

Figure 3 shows the highest value of the effective self-field parameter $2\omega_p^2 / \omega_c^2$ as a function of $\alpha = 2\pi a / L$ for radial confinement. Note that the well-known Brillouin density limit with $2\omega_p^2 / \omega_c^2 = 1$ [5] is recovered by taking $L \to 0$ while holding the effective plasma frequency ω_p fixed.

The results shown in Fig. 3 suggest that a stronger magnetic field is required to confine a beam as it becomes bunched in the axial direction. Work is in progress to examine the full effect of bunching on halo production in high-power PPM klystron amplifiers [6] and to extend the analysis to bunched annular beams.

References

1. See, for example, *Special Issue on High-Power Microwave Generation*, edited by E. Schamiloglu and Y. Y. Lau, IEEE Trans. Plasma Sci. **PS-26**, No. 3 (1998).
2. M. Hess, C. Chen, and R. Pakter, "Three dimensional Green's function description of space charge in intense charged-particle beams," Proc. 1999 Part. Conf. (1999), p. 2752.
3. C. Chen, M. Hess, and R. Pakter, "Electron beam halo formation in periodic permanent focusing klystron amplifiers," in *Intense Microwave Pulses VII*, edited by H. E. Brandt, SPIE Proc. 3041, 34 (2000).
4. M. Hess and C. Chen, "Confinement criterion for a highly bunched beam," Phys. Plasma **7**, 5206 (2000).
5. L. Brillouin, Phys. Rev. **67**, 260 (1945).
6. D. Sprehn, G. Caryotakis, E. Jongewaard, and R. M. Phillips, "Periodic permanent magnetic development for linear collider X-band klystrons," Proc. XIX International Linac Conf. (Argonne National Laboratory Report ANL-98/28, 1998), p. 689.

List of Graduate Students Supported under
AFOSR Grant No. F49620-97-1-0480

Mr. Mark Hess   Graduate Student
MIT Physics Department

Mr. Yoel Fink   Graduate Student
MIT Material Science and Engineering Department

Degree Received: Ph.D
Date: May, 2000
Current Position: Assistant Professor
Department of Material Science and Engineering
MIT

Papers Presented at Technical Conferences
Mechanisms and Control of Chaos and Halos in High-Power Microwave Tubes
AFOSR Grant No. F49620-97-1-0480

The following papers were presented at technical conferences and acknowledged full or partial support by the above referenced grant.

1. "Electron beam halo formation in high-power klystrons," C. Chen, presented at Nonlinear Optics Workshop, University of Arizona, Tucson, September, 1999.

2. "Electron beam halo formation in periodic permanent magnet focusing klystron amplifiers," C. Chen, M. Hess and R. Pakter, presented at SPIE Conference, Intense Microwave Pulses VII, Orlando, Florida, April, 2000.

Reprints on
Mechanisms and Control of Chaos and Halos in High-Power Microwave Tubes
AFOSR Grant No. F49620-97-1-0480

1. M. Hess and C. Chen, "Confinement criterion for a highly bunched beam," Phys. Plasma **7**, 5206 (2000).

2. C. Chen, M. Hess, and R. Pakter, "Electron beam halo formation in periodic permanent focusing klystron amplifiers," in *Intense Microwave Pulses VII*, edited by H. E. Brandt, SPIE Proc. **3641**, 34 (2000).

Confinement criterion for a highly bunched beam

Mark Hess and Chiping Chen

Plasma Science and Fusion Center, Massachusetts Institute of Technology, Cambridge, Massachusetts 02139

The nonrelativistic motion is analyzed for a highly bunched beam propagating through a perfectly conducting cylindrical pipe confined radially by a constant magnetic field parallel to the conductor axis. In the present analysis, the beam is treated as either a thin rod distribution representing a continuous (unbunched) beam or periodic collinear point charges representing a highly bunched beam. Use is made of a Green's function to compute the electrostatic force on the beam due to the induced surface charge in the conductor wall. By analyzing the Hamiltonian dynamics, a criterion is derived for the confinement of unbunched and bunched beams. It is shown that for the confinement of beams with the same charge per unit length, the maximum value of the effective self-field parameter is $2\omega_p^2/\omega_c^2 \cong 2a/L$ for a highly bunched beam with $a \ll L$. This value is significantly lower than the Brillouin density limit for an unbunched beam $2\omega_p^2/\omega_c^2 = 1$. Here, a is the radius of the conducting cylinder, and L is the periodic spacing of the bunches. © *2000 American Institute of Physics.* [S1070-664X(00)02612-4]

I. INTRODUCTION

Confinement and transport of high-intensity charged-particle beams are important subjects in both plasma physics and beam physics.[1,2] It is well-known that for a continuous, non-neutral, charged-particle beam propagating in a uniform magnetic field, the maximum beam density is determined by the so-called Brillouin density limit.[3,4] For nonrelativistic beams, the Brillouin density limit corresponds to the condition $2\omega_p^2/\omega_c^2 = 1$, where $\omega_p = (4\pi q^2 n/m)^{1/2}$ is the nonrelativistic plasma frequency, and $\omega_c = qB/mc$ is the nonrelativistic cyclotron frequency. Although there is a large body of literature on the equilibrium and stability properties of high-intensity continuous non-neutral charged-particle beams, high-intensity bunched beams are rarely discussed in the literature.[5-7]

There is a need to gain a fundamental understanding of high-intensity bunched beams because they are widely employed in high-power microwave (HPM) sources, such as klystrons and traveling wave tubes, as well as in high-intensity particle accelerators such as high-intensity linacs. In both HPM sources and high-intensity particle accelerators, an important problem associated with lack of full beam confinement caused by the bunching of the electron and ion beam in the direction of beam propagation is beam loss, through such mechanisms as beam halo formation.[8-10]

In this paper, we analyze the nonrelativistic motion of a highly bunched beam propagating through a perfectly conducting cylindrical pipe confined radially by a constant magnetic field parallel to the conductor axis. In the present analysis, the beam is treated as either a thin rod distribution representing a continuous (unbunched) beam or periodic collinear point charges representing a highly bunched beam. The Green's function is used to compute the electrostatic force on the beam due to the induced surface charge in the conductor wall. From Hamilton's equations, the radial phase space is studied for both unbunched and bunched beams. In

general, the radial phase space contains both closed orbits (i.e., trapped particle orbits) and untrapped orbits (i.e., orbits which intersect the conductor wall) at sufficiently low beam densities, whereas only untrapped orbits exist at sufficiently high beam densities. By determining the conditions for the disappearance of trapped particle orbits, a criterion for the confinement of a highly bunched beam is derived. It is shown that for the confinement of beams with the same charge per unit length, the maximum value of the effective self-field parameter is $2\omega_p^2/\omega_c^2 \cong 2a/L$ for a highly bunched beam with $a \ll L$, where a is the radius of the conducting cylinder and L is the periodic spacing of the bunches. This result is significantly lower than the Brillouin density limit $2\omega_p^2/\omega_c^2 = 1$ for an unbunched beam.

The paper is organized as follows. In Sec. II, a Green's function model is presented for unbunched and bunched beams, and the electrostatic field produced by the induced surface charge is computed. In Sec. III, the Hamiltonian dynamics of the beam is studied. In Sec. IV, a criterion is derived for the confinement of unbunched and bunched beams. Discussion and conclusions are in Secs. V and VI, respectively.

II. GREEN'S FUNCTION DESCRIPTION OF SPACE CHARGE

The systems we are analyzing consist of periodic space charge in an infinite perfectly conducting cylinder, which is grounded, as shown in Fig. 1. In particular, we investigate the dynamics of two types of periodic space charge. One type is a uniform rod of charge, shown in Fig. 1(a) representing an unbunched beam. Another type is a collinear distribution of charges equally spaced by a distance, L, shown in Fig. 1(b) representing a highly bunched beam. The radius of the cylinder is a, and the distance from the axis that the space charge is displaced is r. We assume that there exists an applied uniform magnetic field $\mathbf{B} = B\hat{e}_z$, and $\hat{e}_z$ denotes the

Phys. Plasmas, Vol. 7, No. 12, December 2000

Confinement criterion for a highly bunched beam   5207
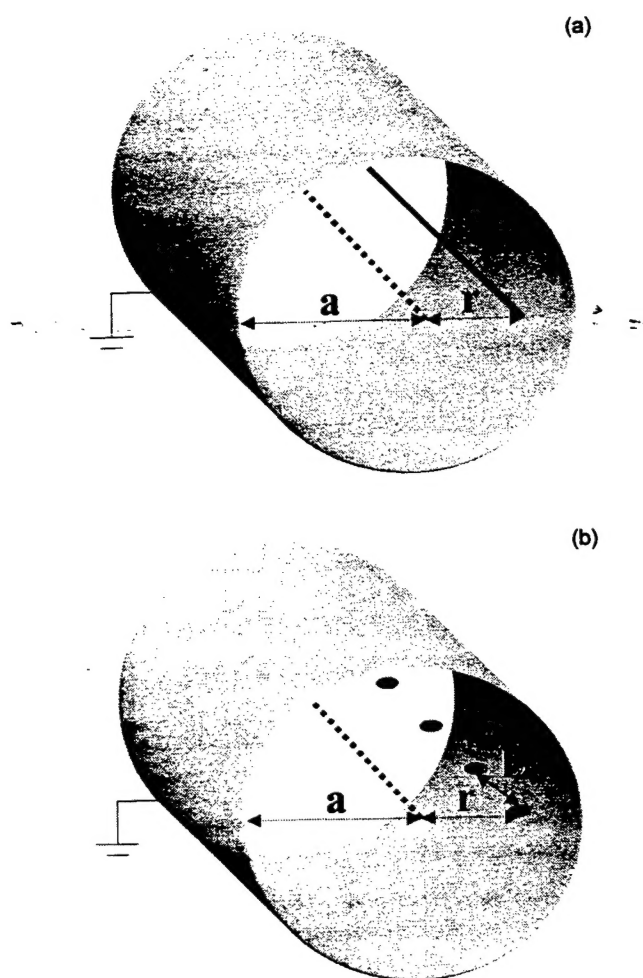
(a)

(b)

FIG. 1. Schematics of (a) line charge and (b) periodic array of charges in a perfectly conducting cylinder.

unit vector parallel to the axis of the conductor. Physically, the two-dimensional (2D) case is recovered from the 3D case by taking the limit $a/L \rightarrow \infty$ for a fixed charge density.

The presence of the periodic space charge induces a charge density, σ, on the surface of the conductor. The induced surface charge provides an electrostatic force on the space charge. We assume that the transverse velocity of the space charge is sufficiently small compared to the speed of light; hence, only the electrostatic force from the conducting wall and the applied magnetic force are non-negligible in the system.

In order to compute the induced surface charge and the electrostatic force, we first formulate a Green's function, which is the electrostatic potential inside the entire cylinder for a given distribution of unit charge(s). In cgs units, the Green's function, G, satisfies the Laplace's equation

$$\nabla^2 G = -4\pi\rho(\mathbf{x}-\mathbf{x}'),\qquad(1)$$

where the primed coordinates denote the position of the charge(s) and the unprimed coordinates denote the point of observation. For the 2D rod of charge

$$\rho(\mathbf{x}-\mathbf{x}')=\frac{1}{r}\delta(r-r')\,\delta(\theta-\theta'),\qquad(2)$$

while for the 3D collinear distribution

$$\rho(\mathbf{x}-\mathbf{x}')=\frac{1}{r}\delta(r-r')\,\delta(\theta-\theta')\sum_{n=-\infty}^{\infty}\delta(z-z'-nL),\qquad(3)$$

where $\delta(x)$ is the Dirac δ function.

The Green's function for both distributions satisfies three other criteria; it must be both rotationally invariant by 2π and translationally invariant by nL in the unprimed coordinates, and the function must be zero at the conductor (Dirichlet condition), i.e.,

$$G|_{\theta+2\pi}=G|_{\theta}$$

$$G|_{z+nL}=G|_{z}\qquad(4)$$

$$G|_{r=a}=0.$$

A solution to (1) can be formed by expanding in terms of eigenfunctions of Laplace's equation in cylindrical coordinates. For the 3D case, we find the solution[11,12]

$$G_{3D}=\frac{2}{L}\sum_{n=-\infty}^{\infty}\sum_{l=-\infty}^{\infty}e^{in(\hat{z}-\hat{z}')}e^{il(\theta-\theta')}$$

$$\times\frac{I_l(n\hat{r}_<)}{I_l(n\alpha)}\{I_l(n\alpha)K_l(n\hat{r}_>)-I_l(n\hat{r}_>)K_l(n\alpha)\},\qquad(5)$$

where

$$\hat{r}=\frac{2\pi r}{L},\quad \hat{r}'=\frac{2\pi r'}{L},\quad \hat{z}=\frac{2\pi z}{L},$$

$$\hat{z}'=\frac{2\pi z'}{L},\quad \alpha=\frac{2\pi\alpha}{L},\qquad(6)$$

and the notation $\hat{r}_{>(<)}$ represents the greater(lesser) of $\hat{r}$ and $\hat{r}'$. Simplification of (5) is possible by summing over the $n=0$ terms, and combining the $n<0$ terms with their positive counterparts, yielding

$$G_{3D}=\frac{1}{L}G_{2D}+\frac{4}{L}\sum_{n=1}^{\infty}$$

$$\times\cos[n(\hat{z}-\hat{z}')]\frac{I_0(n\hat{r}_<)}{I_0(n\alpha)}\{I_0(n\alpha)K_0(n\hat{r}_>)$$

$$-I_0(n\hat{r}_>)K_0(n\alpha)\}+\frac{8}{L}\sum_{n=1}^{\infty}\sum_{l=1}^{\infty}\cos[n(\hat{z}-\hat{z}')]$$

$$\times\cos[l(\theta-\theta')]\frac{I_l(n\hat{r}_<)}{I_l(n\alpha)}\{I_l(n\alpha)K_l(n\hat{r}_>)$$

$$-I_l(n\hat{r}_>)K_l(n\alpha)\},\qquad(7)$$

where G_{2D} represents the solution of (1) for the 2D rod distribution. G_{2D} is given by

$$G_{2D}=\ln\left[\frac{\alpha^2+(\hat{r}_>\hat{r}_</\alpha)^2-2\hat{r}_>\hat{r}_<\cos(\theta-\theta')}{\hat{r}_>^2+\hat{r}_<^2-2\hat{r}_>\hat{r}_<\cos(\theta-\theta')}\right],\qquad(8)$$

which is well known.[13]

Since the Green's function represents the electrostatic potential of a unit charge, we can readily calculate the electric field at the surface of the wall and the induced surface charge density, σ, using the relation

$$\sigma = \frac{\hat{n} \cdot \mathbf{E}|_{\text{surface}}}{4\pi} = \frac{-C\hat{n} \cdot \boldsymbol{\nabla} G|_{\text{surface}}}{4\pi} = \frac{C}{2L} \frac{\partial G}{\partial \hat{r}}\bigg|_{\hat{r}=\alpha}, \quad (9)$$

where $\hat{n}$ denotes the unit vector perpendicular to the surface $(\hat{n} = -\hat{e}_r)$ and $\mathbf{E}$ is the electric field. C is a factor which depends on whether we are solving the 2D or 3D problem. For the 3D problem, C is equal to q, the value of each individual charge. For the 2D problem, C is equal to λ, the charge per unit length of the rod.

For the 2D case, the induced surface charge density is

$$\sigma_{2D} = -\frac{\lambda}{L\alpha}\left[\frac{\alpha^2 - \hat{r}'^2}{\alpha^2 + \hat{r}'^2 - 2\alpha\hat{r}' \cos(\theta - \theta')}\right] = -\frac{\lambda}{L\alpha}\hat{\sigma}_{2D}, \quad (10)$$

while for the 3D case we have

$$\frac{1}{q}\sigma_{3D} = -\frac{\hat{\sigma}_{2D}}{L^2\alpha} - \frac{2}{L^2\alpha}\sum_{n=1}^{\infty} \cos[n(\hat{z} - \hat{z}')]\frac{I_0(n\hat{r}')}{I_0(n\alpha)}$$

$$- \frac{4}{L^2\alpha}\sum_{n=1}^{\infty}\sum_{l=1}^{\infty} \cos[n(\hat{z} - \hat{z}')]$$

$$\times \cos[l(\theta - \theta')]\frac{I_l(n\hat{r}')}{I_l(n\alpha)}. \quad (11)$$

In deriving (11), use has been made of the Wronskian, $I_l(x)K_l'(x) - I_l'(x)K_l(x) = -1/x$.

We are now in a position to compute the electric field, $\mathbf{E}^{\text{self}}$, which is exerted on the charge distribution inside the conductor by the induced surface charge. Because of the system's symmetry in the $\hat{e}_\theta$ and $\hat{e}_z$ directions, the electric field at the charge distribution can only be in the $\hat{e}_r$ direction. Since the sign of the surface charge is opposite to that of the internal charges, the force must be attractive. $\mathbf{E}^{\text{self}}$ can be obtained by integrating the differential electric field vector, evaluated at the charge distribution location, over the entire conductor

$$\mathbf{E}^{\text{self}}(\mathbf{r}') = \oint_{\text{surface}} dS \frac{(\mathbf{r}' - \mathbf{r}_s)\sigma(\mathbf{r}_s)}{|\mathbf{r}' - \mathbf{r}_s|^3}. \quad (12)$$

$\mathbf{r}_s$ is the vector measured from the central axis of the conductor to the point of the differential charge. As will be demonstrated in the Appendix

$$\mathbf{E}_{2D}^{\text{self}}(\mathbf{r}') = \frac{4\pi\lambda}{L}\left(\frac{\hat{r}'}{\alpha^2 - \hat{r}'^2}\right)\hat{e}_{r'}, \quad (13)$$

for the 2D case, and

$$\mathbf{E}_{3D}^{\text{self}}(\mathbf{r}') = E_{3D}^{\text{self}}\hat{e}_{r'},$$

$$E_{3D}^{\text{self}} = \frac{4\pi q}{L^2}\left(\frac{\hat{r}'}{\alpha^2 - \hat{r}'^2}\right)$$

$$+ \frac{8\pi q}{L^2}\sum_{n=1}^{\infty} \frac{nI_0(n\hat{r}')I_0'(n\hat{r}')K_0(n\alpha)}{I_0(n\alpha)}$$

$$+ \frac{16\pi q}{L^2}\sum_{n=1}^{\infty}\sum_{l=1}^{\infty} \frac{nI_l(n\hat{r}')I_l'(n\hat{r}')K_l(n\alpha)}{I_l(n\alpha)} \quad (14)$$

for the 3D system.

III. HAMILTONIAN DYNAMICS

We can investigate the radial dynamics of one rod of charge (2D) or one string of charges (3D) interacting with its self-field (14) and a constant applied magnetic field, $\mathbf{B} = B\hat{e}_z$. In this system, there are no forces in the longitudinal direction. Therefore, we may describe all of the dynamics using a Hamiltonian in the radial and azimuthal directions and set $v_z = 0$ without loss of generality. In particular, the Hamiltonian for transverse motion is given by

$$H = \frac{1}{2m}\left[\left(P_r - \frac{qA_r}{c}\right)^2 + \frac{1}{r^2}\left(P_\theta - \frac{rqA_\theta}{c}\right)^2\right] + q\phi^{\text{self}}, \quad (15)$$

where $\mathbf{P}$ is the canonical momentum, $\mathbf{A} = (rB/2)\hat{e}_\theta$ is the vector potential, and

$$\phi^{\text{self}} = -\int_0^r E^{\text{self}} dr. \quad (16)$$

For the 2D system, we can set $m = \rho L$ where ρ is the mass density of the rod, and $q = \lambda L$. Dividing by L on both sides of (15) yields a Hamiltonian per unit length, which correctly describes the 2D dynamics. Applying Hamilton's equations to (15) gives the following set of normalized equations:

$$\frac{d\hat{r}}{d\tau} = \hat{P}_r, \quad \frac{d\hat{P}_r}{d\tau} = \frac{\hat{P}_\theta^2}{\hat{r}^3} - \hat{r} + \xi\hat{E}^{\text{self}},$$

$$\frac{d\theta}{d\tau} = \frac{\hat{P}_\theta}{\hat{r}^2} - 1, \quad \frac{d\hat{P}_\theta}{d\tau} = 0, \quad (17)$$

where normalized variables and parameters are defined by

$$\tau = \omega_L t, \quad \hat{P}_r = \frac{2\pi P_r}{mL\omega_L}, \quad \hat{P}_\theta = \left(\frac{2\pi}{L}\right)^2 \frac{P_\theta}{m\omega_L}$$

$$\hat{E}^{\text{self}} = \frac{L^2 E^{\text{self}}}{4\pi q}, \quad \xi = \frac{32\pi^2 mc^2}{L^3 B^2}, \quad \omega_L = \frac{qB}{2mc}, \quad (18)$$

and ω_L represents the Larmor frequency. From (17), it is obvious that the canonical angular momentum is conserved. Combining the first two equations in (17), and denoting initial conditions with a subscript 0, we can find an expression relating the canonical radial momentum with the radial position

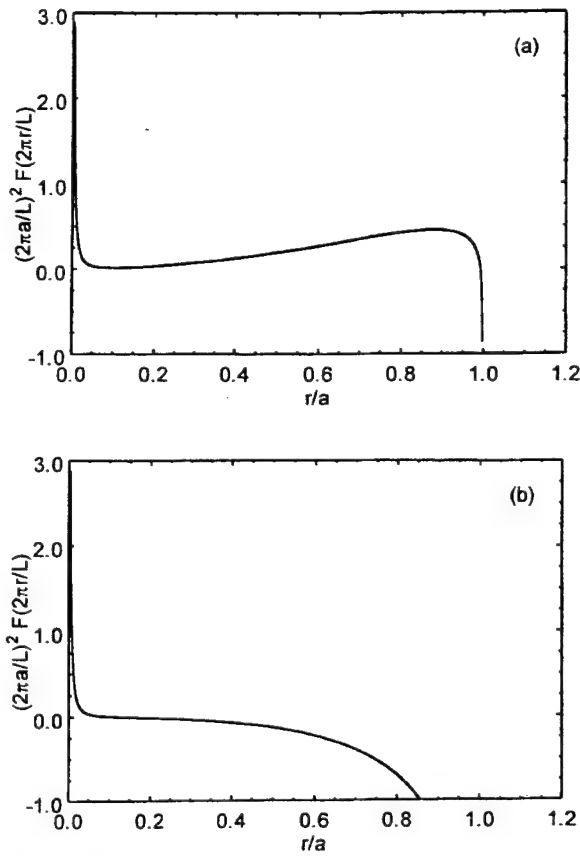$$\hat{P}_r = \pm\sqrt{\hat{P}_{r0}^2 + F(\hat{r}_0) - F(\hat{r})}, \quad (19)$$

Phys. Plasmas, Vol. 7, No. 12, December 2000

Confinement criterion for a highly bunched beam   5209

FIG. 2. Plots of the effective potential $F(\hat{r})$ vs $\hat{r}$ in the 2D system for the choices of system parameters corresponding to: (a) $\xi/\alpha^2 = 0.5$ and $\hat{P}_\theta/\alpha^2 = 0.01$, and (b) $\xi/\alpha^2 = 3.0$ and $\hat{P}_\theta/\alpha^2 = 0.01$.
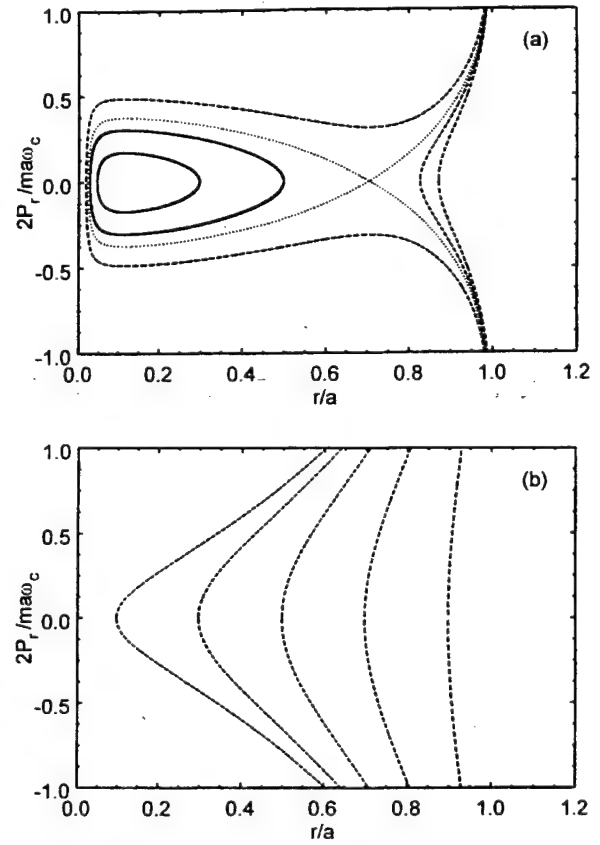

FIG. 3. Plots of the radial phase space in the 2D system for the two cases with the same choices of the system parameters as those shown in Figs. 2(a) and 2(b).

where F represents an effective potential energy, and is given by

$$F(\hat{r}) = \frac{\hat{P}_\theta^2}{\hat{r}^2} + \hat{r}^2 + \xi \ln\left(1 - \frac{\hat{r}^2}{\alpha^2}\right) \qquad (20)$$

for the 2D case, while

$$F(\hat{r}) = \frac{\hat{P}_\theta^2}{\hat{r}^2} + \hat{r}^2 + \xi \ln\left(1 - \frac{\hat{r}^2}{\alpha^2}\right) - 2\xi \sum_{n-1}^{\infty} \frac{K_0(n\alpha)}{I_0(n\alpha)} I_0^2(n\hat{r})$$

$$- 4\xi \sum_{n-1}^{\infty} \sum_{l-1}^{\infty} \frac{K_l(n\alpha)}{I_l(n\alpha)} I_l^2(n\hat{r}) \qquad (21)$$

for the 3D case. Making use of the asymptotic properties of the modified Bessel functions, it is readily shown that in the limit $a/L \rightarrow \infty$, $F(\hat{r})$ in (21) for the 3D case approaches $F(\hat{r})$ in (20) for the 2D case. Therefore, the analysis of confinement in the 2D system will be fully recovered in the 3D analysis in the $a/L = \infty$ limit.

Figures 2(a) and 2(b) show $F(\hat{r})$ plotted for two different sets of values of $(\xi, \hat{P}_\theta)$ for the 2D system. There are two possible behaviors for this function to have. In Fig. 2(a), there is a kink (i.e., the function has one local minimum and one local maximum), while for Fig. 2(b) the function is monotonically decreasing. A function, $F(\hat{r})$, with a kink leads to a radial phase space $(\hat{r}, \hat{P}_r)$, as is illustrated in Fig. 3(a), which contains both trapped and untrapped particle or-

bits. An untrapped particle orbit will result in the particle eventually being lost to the conductor wall, whereas a trapped orbit corresponds to a particle confined inside the perfectly conducting cylinder. A monotonically decreasing function as in Fig. 2(b) will produce a phase space such as Fig. 3(b), which contains only untrapped particle orbits.

To illustrate the 3D effects (i.e., effects of beam bunching), we compare the phase space for the 3D case in Figs. 4(a) and 4(b) with the 2D case shown in Fig. 3. In particular, Fig. 4(a), which has only untrapped orbits, has the same ξ and $\hat{P}_\theta$ values as Fig. 3(a), illustrating the added effect of the electric field in the 3D regime. However, trapped particle orbits do exist at lower values of ξ such as for the value of ξ shown in Fig. 4(a).

IV. CONDITIONS FOR CONFINEMENT

The complete criterion for trapped particle orbits is threefold: (a) $F(\hat{r})$ must have a kink; (b) the initial particle radius must be chosen between the local maximum of $F(\hat{r})$ and the other point on $F(\hat{r})$ corresponding to the same value; and (c) the initial radial momentum must be sufficiently small, such that

$$\hat{P}_{r0}^2 \leqslant F(\hat{r}_0) - F(\hat{r})|_{\min}. \qquad (22)$$

The most important of the three criteria for trapped particle orbits is the first. We therefore determine the region in parameter space $(\alpha, \xi, \hat{P}_\theta)$ space for both the 2D and 3D

5210   Phys. Plasmas, Vol. 7, No. 12, December 2000
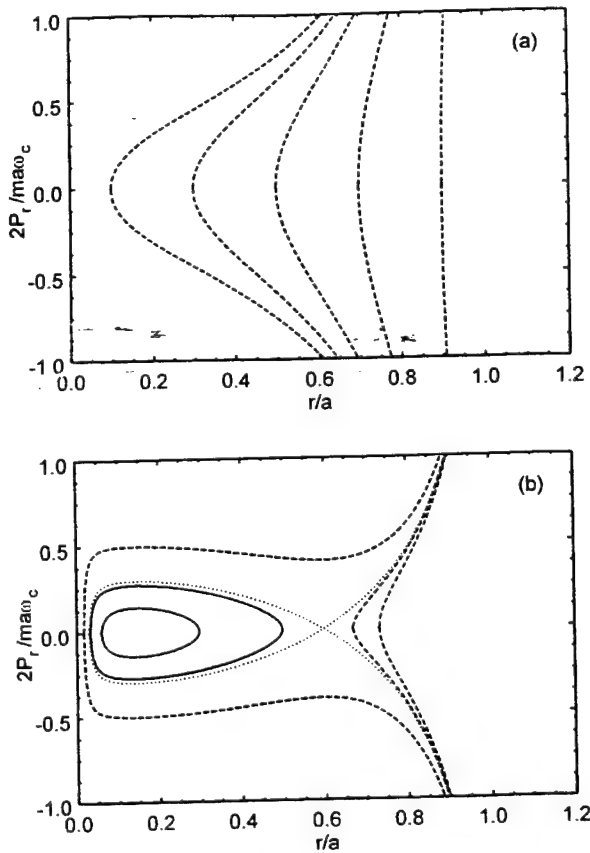
M. Hess and C. Chen

FIG. 4. Plots of the radial phase space in the 3D system for the choices of system parameters corresponding to: (a) $\xi/\alpha^2=0.5$, $\hat{P}_\theta/\alpha^2=0.01$ and $\alpha=1.0$. and (b) $\xi/\alpha^2=0.1$. $\hat{P}_\theta/\alpha^2=0.01$ and $\alpha=1.0$.
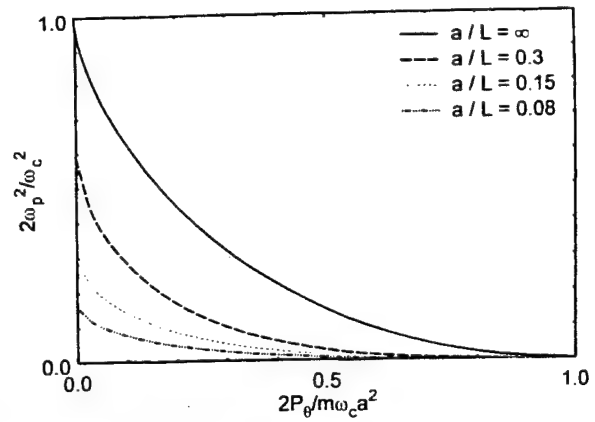

FIG. 5. Plots of the maximum value of the self-field parameter $2\omega_p^2/\omega_c^2$ for confinement as a function of normalized canonical angular momentum $2P_\theta/m\omega_c a^2$ for several values of the aspect ratio a/L in the 3D system. Note that the 2D system corresponds to the limit $a/L=\infty$, and the curve with $a/L=\infty$ is obtained from (30).

systems, such that $F(\hat{r})$ has a kink. In order to find this criterion for $F(\hat{r})$, i.e., that trapped particle orbits may exist, we must look for the conditions such that $F'(\hat{r})=F''(\hat{r})=0$, where $F'(\hat{r})=dF(\hat{r})/d\hat{r}$ and $F''(\hat{r})=d^2F(\hat{r})/d\hat{r}^2$. This represents that transition point between $F(\hat{r})$ being monotonic and nonmonotonic.

A. Confinement for the 2D system

It is evident in (20) that the only increasing term in $F(\hat{r})$ is the $\hat{r}^2$ term and all other terms are decreasing. When $\xi=0$, applying the transition condition $F'(\hat{r})=F''(\hat{r})=0$ yields $|\hat{P}_\theta|=\alpha^2$ at $\hat{r}=\alpha$ for both systems. However, when $\hat{P}_\theta=0$, it follows from (20) that $F(\hat{r})=\hat{r}^2+\xi\ln(1-\hat{r}^2/\alpha^2)$. Expanding $F(\hat{r})$ near $\hat{r}=0$ yields $F(\hat{r})\cong\hat{r}^2(1-\xi/\alpha^2)$. So, $F(\hat{r})$ will not be monotonic at $\hat{r}=0$ for sufficiently small $\hat{P}_\theta$ when the coefficient of the quadratic term is positive (i.e., when $\xi/\alpha^2<1$). Therefore, the necessary conditions for $F(\hat{r})$ to have a kink are $|\hat{P}_\theta|<\alpha^2$ and $\xi/\alpha^2<1$.

Manipulating the equation $F'(\hat{r})=0$ and letting $y=\alpha\hat{r}$, we find that

$$y^6+(\nu-1)y^4+(1-y^2)\mu^2=0, \tag{23}$$

where $\mu=\hat{P}_\theta/\alpha^2$ and $\nu=\xi/\alpha^2$. Because $0<y<1$ $(0<\hat{r}<\alpha)$, we can further simplify (23) by letting $z=y^2$, and obtain

$$G(z)\equiv z^3+(\nu-1)z^2+(1-z)\mu^2=0, \tag{24}$$

where $0<z<1$. Note that $G(0)=\mu^2>0$ and $G(1)=\xi>0$.

It is straightforward to show that $G(z)$ has precisely one zero when the transition point occurs. This statement is equivalent to stating that the minimum of $G(z)$ must be equal to zero, and that the minimum must occur between 0 and 1 for trapping to occur. These conditions yield

$$3z_{min}^2+2(\nu-1)z_{min}-\mu^2=0, \tag{25}$$

$$0<z_{min}=\frac{(1-\nu)+\sqrt{(1-\nu)^2+3\mu^2}}{3}<1, \tag{26}$$

$$z_{min}^3+(\nu-1)z_{min}^2+(1-z_{min})\mu^2=0, \tag{27}$$

where z_{min} is the minimum of G.

Substituting (26) into (27) and solving for μ with the aid of (25) yields two possible solutions

$$\mu^2=\mu_+^2, \quad \mu^2=\mu_-^2, \tag{28}$$

where

$$8\mu_\pm^2=27-18(1-\nu)-(1-\nu)^2$$
$$\pm\sqrt{[27-18(1-\nu)-(1-\nu)^2]^2-64(1-\nu)^3}. \tag{29}$$

However, the inequality (26) yields $\mu^2<2\nu+1$, and by graphical inspection only $\mu^2<\mu_-^2$ is possible. We find that for the 2D system, the following inequality must be satisfied for trapped particle orbits to occur:

$$8\mu^2\leq27-18(1-\nu)-(1-\nu)^2$$
$$-\sqrt{[27-18(1-\nu)-(1-\nu)^2]^2-64(1-\nu)^3}. \tag{30}$$

Note that since μ and ν are both independent of L, (30) is also independent of L. Equation (30) is plotted later in Fig. 5 in terms of normalized P_θ and the effective plasma frequency, as we compare the 2D case with the 3D case.

Since the effective density of particles for both systems is given by $n=(\pi a^2 L)^{-1}$, we can relate ξ/α^2 to the effective plasma frequency $\omega_p=(4\pi n q^2/m)^{1/2}$ (where $q=\lambda L$),

Phys. Plasmas, Vol. 7, No. 12, December 2000

Confinement criterion for a highly bunched beam   5211

and the cyclotron frequency $\omega_c = qB/mc$ by $\xi/\alpha^2 = 2\omega_p^2/\omega_c^2$, which is the familiar self-field parameter. As shown in Fig. 5, the maximum of the self-field parameter occurs at $|\hat{P}_\theta| = 0$, and the maximum value is $2\omega_p^2/\omega_c^2 = 1$. Therefore, the criterion for the confinement is

$$2\omega_p^2/\omega_c^2 \leqslant 1. \tag{31}$$

Note that $\omega_p^2 = \omega_c^2/2$ corresponds to the Brillouin density limit.[3,4]

B. Confinement for the 3D system

For the 3D system when $\hat{P}_\theta = 0$, we can expand (21) near $\hat{r} = 0$ and find that the lowest order nonconstant term, the quadratic term, will be positive when

$$1 - \xi/\alpha^2 - \xi\sum_{n=1}^{\infty} n^2 \left[\frac{K_0(n\alpha)}{I_0(n\alpha)} + \frac{K_1(n\alpha)}{I_1(n\alpha)} \right] \geqslant 0. \tag{32}$$

By utilizing a formula related to the Wronskian, $I_m(z)K_{m+1}(z) + I_{m+1}(z)K_m(z) = 1/z$, we can simplify (32) to

$$\xi \leqslant \frac{\alpha^2}{1 + \Sigma_{n=1}^{\infty} \dfrac{n\alpha}{I_0(n\alpha)I_1(n\alpha)}}. \tag{33}$$

The upper bound on the self-field parameter for the 3D system also occurs at $|\hat{P}_\theta| = 0$; hence, the criterion for confinement is

$$\frac{2\omega_p^2}{\omega_c^2} \leqslant \frac{1}{1 + \Sigma_{n=1}^{\infty} \dfrac{n\alpha}{I_0(n\alpha)I_1(n\alpha)}}. \tag{34}$$

Figure 5 illustrates a few of the critical transition curves in a normalized P_θ and $2\omega_p^2/\omega_c^2$ space. In obtaining the results in Fig. 5, we use Newton's method to simultaneously solve the equations, $F'(\hat{r}) = F''(\hat{r}) = 0$ for fixed values of $\hat{r}$ and α. Seed values are given to ξ and $\hat{P}_\theta$, and convergence of these values typically occurs within five iterations. Because the 2D system corresponds to the limit $a/L \to \infty$ as discussed in Sec. III, the transition curve for $a/L = \infty$ is identical to the results predicted by (30).

Figure 6 shows a plot of the upper bounds for transition to occur in the 2D and 3D systems. The upper bounds are precisely the intersections of the curves in Fig. 5 with the $P_\theta = 0$ axis.

Before concluding this section, we consider the following two limits of (34). Expanding (34) in the limit $\alpha \gg 1$ (i.e., a nearly unbunched beam) and $I_0(n\alpha) \approx I_1(n\alpha) \approx e^{n\alpha}/(2\pi n\alpha)^{1/2}$, we obtain

$$\frac{2\omega_p^2}{\omega_c^2} \cong 1 - 2\pi\alpha^2 e^{-2\alpha} = 1 - \frac{8\pi^3 a^2}{L^2} e^{-4\pi a/L}, \tag{35}$$

which shows that the system asymptotically approaches the 2D system's Brillouin flow limit for large a/L. The other important limit of (34), $\alpha \ll 1$ (i.e., a strongly bunched beam), may be solved numerically, and yields
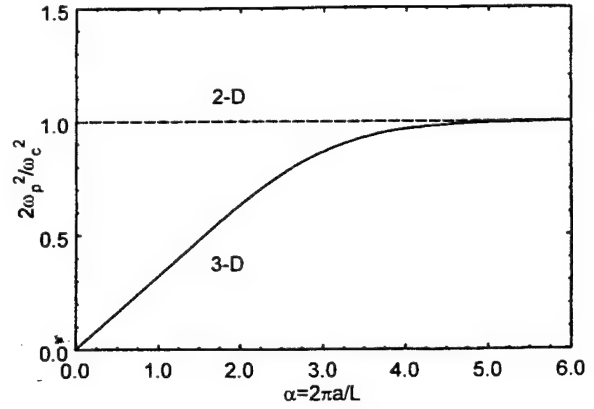

FIG. 6. Plots of the maximum value of the self-field parameter $2\omega_p^2/\omega_c^2$ for confinement as a function of the aspect ratio a/L for $P_\theta = 0$ in both the 2D and 3D systems.

$$\frac{2\omega_p^2}{\omega_c^2} \cong \frac{\alpha}{\pi} = \frac{2a}{L}, \tag{36}$$

which is significantly lower than the Brillouin density limit.

V. DISCUSSION

We have ignored the realistic effect of a finite bunch size in our present model. Incorporating such an effect would reduce the stringent beam confinement criterion placed on the self-field parameter. Qualitatively, both the beam space charge and the induced surface charges would be less dense, and therefore the beam would experience a reduced electric field force from the conducting wall and the other bunches.

A separate effect for a finite charge bunch would be the evolution of the bunch shape. In order to evaluate the importance of such an effect relative to the beam loss mechanism just described, it is necessary to compare their time scales. We will now give an order of magnitude estimate for the escape time (i.e., the time needed for a particle to escape to the wall).

For simplicity, assume that the particle has no canonical angular momentum ($\hat{P}_\theta = 0$), and the particle is initially at the center of the conductor ($\hat{r} = 0$). We will assume that the initial radial momentum is nonzero, but relatively small ($0 < \hat{P}_{r0}^2 < \alpha^2 \ll \xi$). Using (17) and ignoring the 3D correction terms $F(\hat{r})$, we obtain

$$\tau = \int_0^\alpha \frac{d\hat{r}}{\hat{P}_r} = \int_0^1 \frac{d\chi}{[\hat{P}_{r0}^2/\alpha^2 - \chi^2 - \xi/\alpha^2 \ln(1-\chi^2)]^{1/2}}, \tag{37}$$

where $\chi = \hat{r}/\alpha$. Therefore, the escape time is $t = \tau/\omega_L \sim (\xi/\alpha^2)^{-1/2}/\omega_L \sim \omega_p^{-1}$.

We can obtain an order of magnitude for the evolution time, by considering the dynamics of only one uniform spherical bunch of radius, R, charge, q, and mass, m, with no conductor present. Using Coulomb's law and the Lorentz force law, we find that

$$\frac{d^2R}{dt^2} = \frac{q^2}{mR^2}. \tag{38}$$

5212   Phys. Plasmas, Vol. 7, No. 12, December 2000

M. Hess and C. Chen

Equation (38) implies that the evolution time scale is of the order $(mR^3/q^2)^{1/2}$. Assuming the density is of the order $(4\pi R^3/3)^{-1}$, then the evolution time is of the order ω_p^{-1}. Hence, the effect of the bunch shape evolution is, in general, not negligible compared to the beam loss mechanism. Therefore, a detailed investigation of the effect of finite bunch size is required to quantify the confinement of moderately bunched beams.

VI. SUMMARY

In the present paper, we have derived confinement criteria for a highly bunched beam and an unbunched beam propagating down a perfectly conducting cylinder with an applied magnetic field. We have modeled these two systems by approximating the unbunched beam as a rod of charge and the bunched beam as collinear periodic charges. For these two models, we have derived the equations of transverse motion from the Hamiltonian.

The criteria have been obtained by examining the properties of the beam's radial phase space. There are two possible phase spaces, one which allows trapped particle orbits and one which does not. The difference between the two is shown to be caused by the behavior of an effective radial potential (i.e., whether it has a kink or not). When varying the three parameters $(\alpha, \xi, \hat{P}_\theta)$ in the system, the behavior of the effective potential undergoes a critical transition.

The values of $(\alpha, \xi, \hat{P}_\theta)$ where the critical transition occurs yield an upper bound on the self-field parameter $2\omega_p^2/\omega_c^2 \equiv \xi/\alpha^2$ for which trapped particle orbits exist. For an unbunched beam, the upper bound on the self-field parameter has been shown to be $2\omega_p^2/\omega_c^2 \leqslant 1$, which is precisely the Brillouin density limit. For a bunched beam, the maximum value of the self-field parameter is given in (34). The limit on the self-field parameter will always be less for the bunched beam than for the unbunched beam due to the higher local density of internal charges and induced surface charges, which contribute a higher electric field force.

The results reported in this paper are applicable to a relativistic charged-particle beam by a proper application of the Lorentz transformation from the laboratory frame to the frame of reference moving with the beam. Finally, it is anticipated that the results in this paper will provide a useful insight into the confinement of high-intensity bunched beams in linear accelerators as well as in high-power microwave sources such as klystrons.

APPENDIX: CALCULATION OF THE ELECTROSTATIC SELF-FIELD

When calculating the self-field force, we may assume that $\theta' = \hat{z}' = 0$, without loss of generality, and express $\mathbf{r}'$

$= (L/2\pi)\hat{r}'\hat{e}_{x'}$ and $\mathbf{r}_s = (L\alpha \cos\theta/2\pi)\hat{e}_x + (L\alpha \sin\theta/2\pi)\hat{e}_y + (L\hat{z}/2\pi)\hat{e}_z$. Since $E_z(\mathbf{r}') = E_\theta(\mathbf{r}') = 0$ by the symmetries of the system in the longitudinal and azimuthal directions, we need only consider the force along the direction of $\hat{e}_{r'} = \hat{e}_{x'}$. Making use of the expressions

$$\frac{(\mathbf{r}' - \mathbf{r}_s)\cdot\hat{e}_{x'}}{|\mathbf{r}' - \mathbf{r}_s|^3} = -\left(\frac{2\pi}{\alpha L}\right)^2 \frac{\cos\theta - \dfrac{\hat{r}'}{\alpha}}{\left(1 + \dfrac{\hat{r}'^2}{\alpha^2} + \dfrac{\hat{z}^2}{\alpha^2} - 2\dfrac{\hat{r}'}{\alpha}\cos\theta\right)^{3/2}}$$

and $dS = \alpha\, dz\, d\theta = (L/2\pi)^2\alpha\, d\hat{z}\, d\theta$, we may express (12) as

$$E^{\text{self}} = -4\int_0^\infty d\eta \int_0^\pi \frac{(\cos\theta - \beta)\sigma\, d\theta}{(1 + \beta^2 + \eta^2 - 2\beta\cos\theta)^{3/2}}, \quad (A1)$$

where $\eta = \hat{z}/\alpha$ and $\beta = \hat{r}'/\alpha$, and we have also used the longitudinal and azimuthal symmetries to change the limits of integration.

Substituting (10) into (A1), we find that the self-electric field produced by the 2D induced surface charge at the line charge is

$$\begin{aligned}
E_{2D}^{\text{self}} &= \frac{4(1-\beta^2)\lambda}{L\alpha}\int_0^\pi \frac{d\theta(\cos\theta - \beta)}{(1 + \beta^2 - 2\beta\cos\theta)} \\
&\quad \times \int_0^\infty \frac{d\eta}{(1 + \beta^2 + \eta^2 - 2\beta\cos\theta)^{3/2}} \\
&= \frac{4\pi\lambda}{L}\frac{\hat{r}'}{\alpha^2 - \hat{r}'^2} \quad (A2)
\end{aligned}$$

which is identical to (13). This result can also be obtained easily using the method of images.[13]

Of course, the first term in (14) corresponds to the 2D component, which we have just derived. Substituting (11) into (A1), we can express the self-electric field produced by the 3D induced surface charge at the point charge as

$$\begin{aligned}
E_{3D}^{\text{self}} &= \frac{4\pi q}{L^2}\left(\frac{\hat{r}'}{\alpha^2 - \hat{r}'^2}\right) + \frac{8q}{\alpha L^2}\sum_{n=1}^\infty \frac{I_0(n\hat{r}')\Theta_{n0}}{I_0(n\alpha)} \\
&\quad + \frac{16q}{\alpha L^2}\sum_{n=1}^\infty \sum_{l=1}^\infty \frac{I_l(n\hat{r}')\Theta_{nl}}{I_l(n\alpha)}, \quad (A3)
\end{aligned}$$

where

$$\begin{aligned}
\Theta_{nl} &= \int_0^\pi \int_0^\infty \frac{\cos(n\alpha\eta)\cos(l\theta)(\cos\theta - \beta)d\eta\, d\theta}{(1 + \beta^2 + \eta^2 - 2\beta\cos\theta)^{3/2}} \\
&= \frac{\partial}{\partial\beta}\int_0^\pi \int_0^\infty \frac{\cos(n\alpha\eta)\cos(l\theta)d\eta\, d\theta}{(1 + \beta^2 + \eta^2 - 2\beta\cos\theta)^{1/2}}
\end{aligned}$$

Phys. Plasmas, Vol. 7, No. 12, December 2000

Confinement criterion for a highly bunched beam   5213

$$= \frac{\partial}{\partial \beta} \int_0^\pi K_0(n\alpha\sqrt{1+\beta^2-2\beta\cos\theta})\cos(l\theta)d\theta$$

$$= \frac{\partial}{\partial \beta} \int_0^\pi \left[I_0(n\alpha\beta)K_0(n\alpha) \right.$$

$$\left. + 2\sum_{p=1}^\infty I_p(n\alpha\beta)K_p(n\alpha)\cos(p\theta) \right]\cos(l\theta)d\theta$$

$$= \pi K_l(n\alpha)\frac{\partial}{\partial \beta}I_l(n\alpha\beta) = \pi n\alpha K_l(n\alpha)I_l'(n\hat{r}').$$

$$\tag{A4}$$

In the third step in (A4), we made use of the relation[14]

$$\int_0^\infty \frac{\cos(ax)dx}{\sqrt{b^2+x^2}} = K_0(ab),$$

while in step 4 we used the formula[15]

$$K_0(\sqrt{a^2+b^2-2ab\cos\theta})$$

$$= I_0(a)K_0(b) + 2\sum_{p=1}^\infty I_p(a)K_p(b)\cos(p\theta),$$

$$0 \le a < b.$$

Substituting (A4) into (A3) yields (14).

[1] R. C. Davidson, *Physics of Nonneutral Plasmas* (Addison-Wesley, Reading, MA, 1990).

[2] M. Reiser, *Theory and Design of Charged Particle Beams* (Wiley, New York, 1994).

[3] L. Brillouin, Phys. Rev. **67**, 260 (1945).

[4] See, for example, Ref. 1, Chap. 1, p. 545.

[5] F. J. Sacherer, IEEE Trans. Nucl. Sci. **NS-18**, 1105 (1971).

[6] J. J. Barnard and S. M. Lund, in *Proceedings of the Particle Accelerator Conference*, edited by M. Comyn (Institute of Electrical and Electronics Engineers, Piscataway, NJ, 1997), p. 1929.

[7] R. L. Gluckstern, A. V. Fedotov, S. Kurennoy, and R. Ryne, Phys. Rev. E **58**, 4977 (1998).

[8] C. Chen and R. Pakter, Phys. Plasmas **5**, 2203 (2000).

[9] R. Pakter and C. Chen, "Electron beam halo formation in high-power periodic permanent magnet focusing klystron amplifiers," IEEE Trans. Plasma Sci. (in press).

[10] C. Chen and R. Pakter, in *Intense Microwave Pulses VI*, edited by H. E. Brandt, SPIE Proc. **3702**, 21 (1999).

[11] J. D. Jackson, *Classical Electrodynamics*, 2nd ed. (Wiley, New York, 1975), Chap. 3.

[12] M. Hess, R. Pakter, and C. Chen, in *Proceedings of the Particle Accelerator Conference*, edited by A. Luccio and W. Mackay (Institute of Electrical and Electronics Engineers, Piscataway, NJ, 1999), p. 2752.

[13] G. Barton, *Elements of Green's Functions and Propagation* (Oxford University Press, New York, 1995), pp. 412–416.

[14] I. S. Gradshteyn and I. M. Ryzhik, *Table of Integrals, Series, and Products*, 5th ed. (Academic, London, 1994), p. 464.

[15] A. Gray and G. B. Mathews, *A Treatise on Bessel Functions and Their Applications to Physics*, 2nd ed. (MacMillan, London, 1952), p. 74.

ELECTRON BEAM HALO FORMATION IN PERIODIC PERMANENT MAGNET FOCUSING KLYSTRON AMPLIFIERS

C. Chen, M. Hess and R. Pakter
Plasma Science and Fusion Center
Massachusetts Institute of Technology
Cambr˙ ˌge, MA 02139

ABSTRACT

Electron beam halo formation is studied as a potential mechanism for electron beam losses in high-power periodic permanent magnet focusing klystron amplifiers. In particular, a two-dimensional self-consistent electrostatic model is used to analyze equilibrium beam transport in a periodic magnetic focusing field in the absence of radio-frequency signal, and the behavior of a high-intensity electron beam under a current-oscillation-induced mismatch between the beam and the periodic magnetic focusing field. Detailed simulation results are presented for choices of system parameters corresponding to the 50 MW, 11.4 GHz periodic permanent magnet (PPM) focusing klystron experiment performed at the Stanford Linear Accelerator Center (SLAC). It is found from the self-consistent simulations that sizable halos appear after the beam envelope undergoes several oscillations, and that the residual magnetic field at the cathode plays an important role in delaying the halo formation process. Finally, a confinement criterion is obtained for a highly bunched beam propagating through a perfectly conducting drift tube in a uniform magnetic field.

I. INTRODUCTION

One of the main thrusts in high-power microwave (HPM) research is to overcome the problem of radio-frequency (RF) pulse shortening [1,2]. Several mechanisms of RF pulse shortening have been proposed [3], ranging from plasma formation at various locations in the device to nonlinear effects at the RF output section [4-7]. However, few of them have been fully verified in terms of theory, simulation and experiment. In this paper, we discuss halos around high-intensity electron beams as a mechanism by which electron beam loss and subsequent plasma formation may occur in high-power klystron amplifiers.

From the point of view of beam transport in a periodic or uniform solenoidal focusing field, there are two main processes for halo formation in high-intensity electron beams. One process is caused by a mismatch in the root-mean-square (rms) beam envelope [8], and the other is due to a mismatch in the electron phase-space distribution [9]. Both processes can occur when the beam intensity is sufficiently high so that the electron beam becomes space-charge-dominated. The purpose of this paper is to show that the former is responsible for electron beam halos in high-power klystron amplifiers.

For a periodic solenoidal focusing channel with periodicity length S and vacuum phase advance σ_0, a *space-charge-dominated electron beam* satisfies the condition [8]

$$\frac{SK}{4\sigma_0\varepsilon} = 2.9 \times 10^{-5} \frac{1}{\sigma_0}\left(\frac{S}{\varepsilon_n}\right)\frac{I_b}{\gamma_b^2\beta_b^2} > 1, \tag{1}$$

where $K = 2e^2 N_b / \gamma_b^3\beta_b^2 mc^2$ is the normalized self-field perveance, I_b is the electron beam current in amperes, $\varepsilon_n = \gamma_b\beta_b\varepsilon$ is the normalized rms emittance in meter-radians, and S is in meters. In the expressions for the self-field perveance K and the normalized rms emittance ε_n, N_b is the number of electrons per unit axial length, m and $-e$ are the electron rest mass and charge, respectively, c is the speed of light in *vacuo*, and $\gamma_b = \left(1 - \beta_b^2\right)^{-1/2}$ is the characteristic relativistic mass factor for the electrons. The emittance is essentially the beam radius times a measure of randomness in the transverse electron motion. For a uniform density beam with radius a and temperature T_b, the normalized rms emittance ε_n is given by

$$\varepsilon_n = \gamma_b\beta_b\varepsilon = \frac{a}{2}\left(\frac{\gamma_b k_B T_b}{mc^2}\right)^{1/2}, \tag{2}$$

where k_B is the Boltzmann constant.

In particular, we study equilibrium beam transport in a periodic magnetic focusing field in the absence of RF signal and the behavior of a high-intensity electron beam under a current-oscillation-induced mismatch between the beam and the periodic magnetic focusing field, using a two-dimensional self-consistent electrostatic model. Detailed simulation results are presented for choices of system parameters corresponding to the 50 MW, 11.4 GHz periodic permanent magnet (PPM) focusing klystron experiment [10] performed at the Stanford Linear Accelerator Center (SLAC). It is found from the self-consistent simulations that sizable halos appear after the beam envelope undergoes several oscillations, and that the residual magnetic field at the cathode plays an important role in delaying the halo formation process. Preliminary results of this study were reported earlier [11], and more detailed results were discussed elsewhere [12,13].

We also study the confinement of a highly bunched beam propagating through a perfectly conducting drift tube in a uniform magnetic field based on the Green's function description of space charge. In the present analysis, a highly bunched beam is treated as a periodic array of point charges, while a unbunched beam is considered as a line charge. By analyzing the equations of motion of a line charge and of a periodic array of point charges, confinement criteria are derived for unbunched and highly bunched beams propagating through a perfectly conducting drift tube in a uniform magnetic field.

The paper is organized as follows. In Section II, a two-dimensional self-consistent model is presented for transverse electrostatic interactions in a high-intensity relativistic electron beam propagating in a periodic focusing magnetic field. In Section III, the equilibrium state for intense electron beam propagation through a PPM focusing field is discussed, the equilibrium (well-matched) beam envelope is determined, and self-consistent simulations of equilibrium beam transport are performed. In Section IV, the effects of large-amplitude charge-density and current oscillations on inducing mismatched beam envelope oscillations are discussed, and use is made of the model presented in Section II to study the process of halo formation in a high-intensity electron beam. The results are compared with the SLAC PPM focusing klystron amplifier

experiment. In Section V, a confinement criterion is obtained for highly bunched beam propagation through a perfectly conducting drift tube in a uniform magnetic field. In Section VI, conclusions are given.

II. MODEL AND ASSUMPTIONS

We consider a high-intensity relativistic electron beam propagating with axial velocity $\beta_b c \hat{e}_z$ through the periodic focusing magnetic field

$$\vec{B}^{ext}(x,y,s) = B_z(s)\hat{e}_z - \frac{1}{2}B_z'(s)\left(x\hat{e}_x + y\hat{e}_y\right),$$ (3)

where $s = z$ is the axial coordinate, $x\hat{e}_x + y\hat{e}_y$ is the transverse displacement from the z-axis, $B_z(s+S) = B_z(s)$, S is the fundamental periodicity length of the focusing field, and the prime denotes derivative with respect to s.

In the present two-dimensional analysis, we treat only the transverse electrostatic interactions in the electron beam. The effects of longitudinal charge-density and current oscillations in the electron beam, which are treated using the relativistic Lorentz equation and full Maxwell equations, will be considered in Section IV. For present purposes, we make the usual thin-beam approximation, assuming that (a) the Budker parameter is small, i.e., $e^2 N_b / \gamma_b mc^2 << 1$, (b) the beam is thin compared with the lattice period S, and (c) the electron motion in the transverse direction is nonrelativistic.

Under the thin beam approximation, the self-consistent electrostatic interactions in the electron beam can be described by a two-dimensional model involving N_p macroparticles (i.e., charged rods). In the Larmor frame, the transverse dynamics of the macroparticles is governed by [8,14]

$$\frac{d^2 x_i}{ds^2} + \kappa_z(s)x_i - \frac{e}{\gamma_b^3 \beta_b^2 mc^2}\frac{\partial}{\partial x_i}\phi^s(x_i,y_i,s) = 0,$$ (4)

$$\frac{d^2 y_i}{ds^2} + \kappa_z(s)y_i - \frac{e}{\gamma_b^3 \beta_b^2 mc^2}\frac{\partial}{\partial y_i}\phi^s(x_i,y_i,s) = 0,$$ (5)

where $i = 1, 2, ..., N_p$, and the focusing parameter $\kappa_z(s)$ and self-field potential $\phi^s(x_i,y_i,s)$ are defined by

$$\kappa_z(s) = \left[\frac{eB_z(s)}{2\gamma_b\beta_c mc^2}\right]^2 = \left[\frac{\Omega_c(s)}{2\beta_b c}\right]^2,$$ (6)

$$\phi^s(x_i,y_i,s) = -\frac{eN_b}{N_p}\sum_{j=1(j\neq i)}^{N_p}\ln\left\{\frac{\left[x_i - x_j\right]^2 + \left[y_i - y_j\right]^2}{\left[x_i - x_j r_w^2 / r_j^2\right]^2 + \left[y_i - y_j r_w^2 / r_j^2\right]^2}\right\},$$ (7)

respectively. Here, $\Omega_c(s)$ is the (local) relativistic cyclotron frequency associated with the axial magnetic field $B_z(s)$, and $r_i \equiv (x_i^2 + y_i^2)^{1/2}$. The beam is assumed to propagate inside a perfectly conducting cylindrical tube of radius r_w, such that the self-field potential satisfies the boundary condition $\phi^s(r_i = r_w, s) = 0$. Note that $\phi^s(x_i, y_i, s)$ is expressed as a sum of the Green's functions for the Poisson's equation for a line charge in the conducting cylindrical tube. Detailed derivations of Eqs. (4)-(7) can be found in [8] for $r_w \rightarrow \infty$.

The two-dimensional self-consistent model described by Eqs. (4) and (5) will be used to simulate equilibrium beam transport in a PPM focusing field in the absence of RF signal (Section III) and electron beam halo formation in the transverse direction induced by large-amplitude longitudinal current oscillations (Section IV).

III. EQUILIBRIUM BEAM TRANSPORT

In the absence of RF signal, the relativistic electron beam propagates through the focusing field in an equilibrium state. In this section, we discuss important properties of the equilibrium beam transport, and present results of our analysis and self-consistent simulations of periodically focused intense electron beam equilibria for choices of system parameters corresponding to those used in the SLAC 50 MW, 11.4 GHz PPM focusing klystron experiment [10].

A. Beam Envelope Equation for a Rigid-Rotor Vlasov Equilibrium

It has been shown previously [15,16] that one of the equilibrium states for the system described by Eqs. (4) and (5) is a rigid rotor Vlasov equilibrium in which the beam density is uniform transverse to the direction of beam propagation. The outermost beam radius $r_b(s) = r_b(s+S)$ obeys the envelope equation [15]

$$\frac{d^2 r_b}{ds^2} + \kappa_z(s) r_b - \frac{K}{r_b} - \frac{\langle \hat{P}_\theta \rangle^2}{r_b^3} - \frac{(4\varepsilon)^2}{r_b^3} = 0, \tag{8}$$

where $\gamma_b \beta_b mc \langle \hat{P}_\theta \rangle$ = constant is the macroscopic canonical angular momentum of the beam at $r = r_b(s)$, and ε is the unnormalized rms emittance associated with the random motion of the electrons. If there is no magnetic field at the cathode, then $\langle \hat{P}_\theta \rangle = 0$. Any residual magnetic field at the cathode will lead to $\langle \hat{P}_\theta \rangle \neq 0$.

We analyze the beam envelope for equilibrium beam transport in the SLAC 50 MW, 11.4 GHz PPM focusing klystron experiment [10]. The system parameters of the experiment are shown in Table 1. To examine the influence of small residual magnetic field on the beam transport, we analyze two different cases shown in Table 2. In Case I, we assume no residual magnetic field at the cathode, such that $\gamma_b \beta_b mc \langle \hat{P}_\theta \rangle = 0$. In Case II, however, a residual field of 6.86 G is assumed, corresponding to a beam with a finite canonical angular momentum given by

$\gamma_b \beta_b mc \langle \hat{P}_\theta \rangle = 4.5 \times 10^{-26}$ Kgm^2/s. The following dimensionless parameters are derived from Table 2: $S^2 \kappa_z(s) = [1.04 \times \sin(2\pi s / S)]^2$ (with $S = 2.1$ cm), $\sigma_0 = 42.3° = 0.738$, $SK/4\sigma_0\varepsilon = 10.1$, and $\langle \hat{P}_\theta \rangle / 4\varepsilon = 0.0$ in Case I and $\langle \hat{P}_\theta \rangle / 4\varepsilon = 6.93$ in Case II.

Figure 1 shows plots of the axial magnetic field $B_z(s)$ and outermost beam radius $r_b(s)$ versus the propagation distance s for Cases I and II. In both cases, the amplitude of well-matched (equilibrium) envelope oscillations about the average beam radius is only about 0.005 mm, as seen in Figs. 1(b) and 1(c).

Table 1. SLAC 50 MW, 11.4 GHz, PPM Focusing Klystron Experiment

Beam Current I_b	190 A
Beam Voltage	464 kV
Cathode Radius	2.86 cm
Cathode Temperature T_b	800°C [†]
Beam Radius	2.38 mm[†]
Pipe Radius	4.7625 mm
Total Tube Length	90.0 cm
Focusing Field Period Length	2.1 cm
PPM Focusing Section Length	42.0 cm
RMS Axial Magnetic Field	1.95 kG

[†] estimated

Table 2. System Parameters Used in the Simulation

| BASIC PARAMETER	CASE I	CASE II
Beam Current I_b	190 A	190 A
Beam Voltage	464 kV	464 kV
Cathode Radius	2.86 cm	2.86 cm
Residual Magnetic Field at Cathode	0.0 G	6.86 G
Cathode Temperature T_b	800°C	800°C
Beam Radius	2.05 mm	2.38 mm
Pipe Radius	9.0 mm	9.0 mm
Total Tube Length	90.0 cm	90.0 cm
Focusing Field Period Length	2.1 cm	2.1 cm
PPM Focusing Section Length	42.0 cm	42.0 cm
RMS Axial Magnetic Field	1.95 kG	1.95 kG
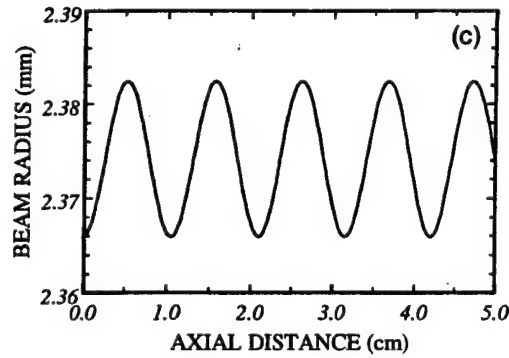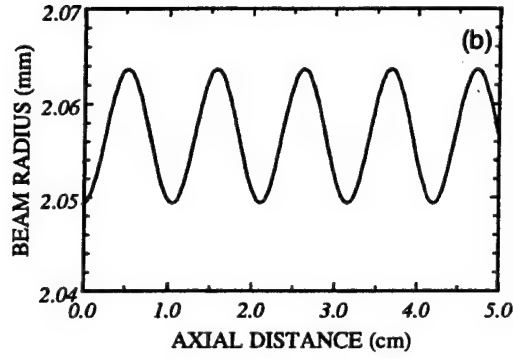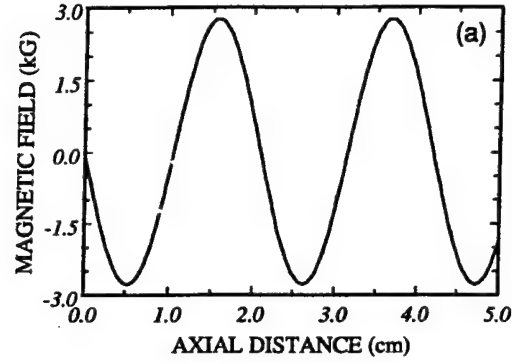
Figure 1. Plots of the axial magnetic field in (a) and outermost beam radius $r_b(s)$ versus the propagation distance s for equilibrium beam propagation corresponding to Case I in (b) and Case II in (c). The dimensionless parameters are: $S^2\kappa_z(s) = [1.04 \times \sin(2\pi s / S)]^2$, $\sigma_0 = 42.3° = 0.738$, $SK / 4\sigma_0\varepsilon = 10.1$, and $\langle \hat{P}_\theta \rangle / 4\varepsilon = 0.0$ in (b) and $\langle \hat{P}_\theta \rangle / 4\varepsilon = 6.93$ in (c).

B. Self-Consistent Simulation of Equilibrium Beam Transport

Self-consistent simulations based on the model described in Sec. II are performed to further investigate the equilibrium beam transport. In the simulations, 4096 macroparticles are used. The macroparticles are loaded according to the rigid-rotor Vlasov distribution [15] with an initial beam radius equal to the equilibrium (matched) beam radius at $s = 0$ [see Figs. 1(b) and 1(c) for Cases I and II, respectively].

Figure 2 shows, respectively, the initial and final phase-space distributions at $s = 0.0$ cm and $s = 42.0$ cm for Case I. Comparing the phase-space plots shown in Figs. 2(e) and 2(f) with the initial phase-space plots in Figs. 2(b) and 2(c), we find an increase in the emittance (randomness) in the transverse electron momentum. The emittance growth is a result of numerical noise in the simulation. However, since the beam dynamics is mostly dictated by space-charge forces for the parameter regime considered here, the emittance growth has little effect on the beam transport properties. In fact, the distribution in the configuration space shown in Fig. 2(d) agrees very well with the initial distribution shown in Fig. 2(a). Moreover, the effective beam radius obtained from the simulation agrees with that obtained from Eq. (8) within 0.2%. In the simulation, no beam loss is detected.
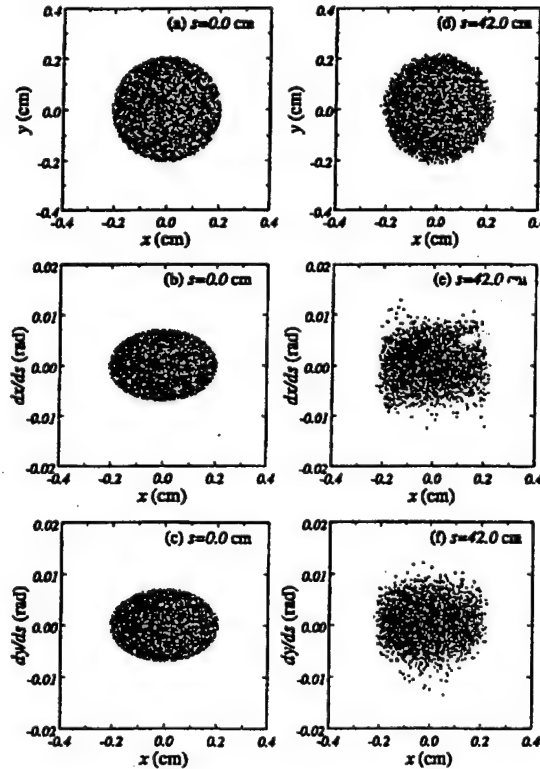

Figure 2.   Plots of the initial and final particle distributions at $s = 0.0$ and 42.0 cm for the equilibrium beam corresponding to the parameters in Case I.
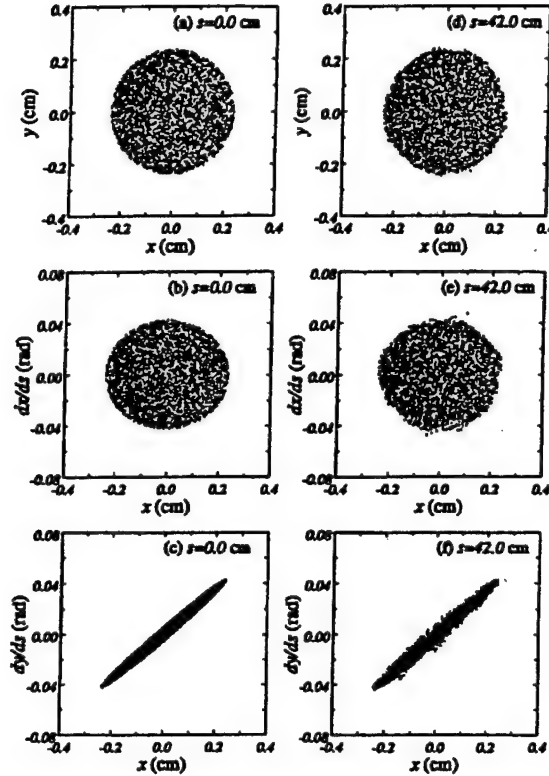
Figure 3.   Plots of the initial and final particle distributions at $s = 0.0$ and 42.0 cm for the equilibrium beam corresponding to the parameters in Case II.

Figure 3 shows, respectively, the initial and final phase-space distributions at $s = 0.0$ cm and $s = 42.0$ cm for Case II. The final distributions shown in Figs. 3(d), 3(e), and 3(f) agree very well with the initial distributions shown in Figs. 3(a), 3(b), and 3(c). In this case, the effects of numerical-noise-induced emittance growth are less pronounced than in Case I (Fig. 2) because the momentum distribution is primarily determined by the finite angular momentum but not by thermal effects. The effective beam radius agrees with Eq. (8) within 0.5%, and no beam loss is detected in the simulation.

C. Phase Space Structure

It is known that the phase space structure for a matched intense beam in a periodic focusing system exhibits nonlinear resonances and chaotic behavior [17]. To determine how sensitive the equilibrium beam transport is against small perturbations for the parameter region of interest, we examine test-particle dynamics subject to the field configuration consisting of the applied focusing field and the equilibrium self-electric and self-magnetic fields. We make use of the Poincaré surface-of-section method to analyze the phase-space structure of test particles. The results are shown in Fig. 4(a) for Case I with $\hat{P}_\theta / 4\varepsilon = 0$, and in Fig. 4(b) for Case II with $\hat{P}_\theta / 4\varepsilon = -0.99$.

In Fig. 4, the successive intersections of 15 test-particle trajectories with the phase space (r, P_r) are plotted every period of the focusing field for 1000 periods. One test particle is initialized at the phase-space boundary of the equilibrium distribution, and the corresponding test-particle orbit is represented by the inner curved arc in Fig. 4(a) and by the innermost contour in Fig. 4(b). The remaining test particles are initialized outside the beam. For both cases shown in Fig. 4, the values of $\hat{P}_\theta$ are chosen such that the boundary of the equilibrium distribution extends to $r = r_b$. Although the space-charge force outside the beam is nonlinear, the phase space is almost entirely regular. The same results showing regularity in phase space structure are obtained for different values of $\hat{P}_\theta$ for Cases I and II.
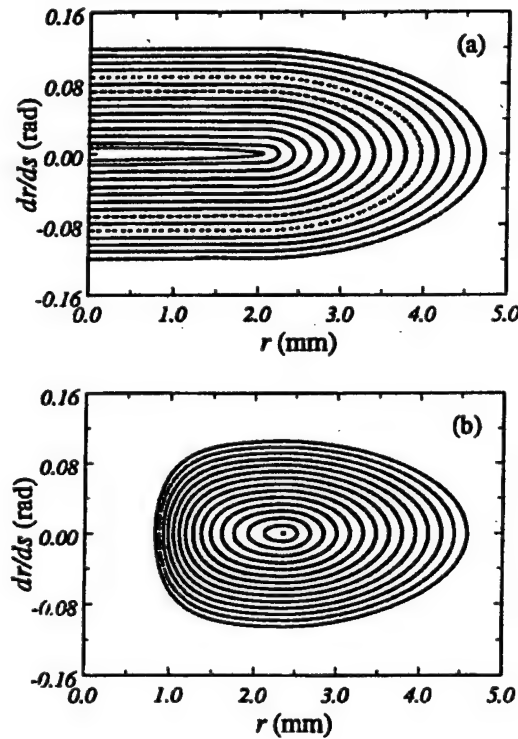

Figure 4. Poincaré surface-of-section plots for 15 test particle trajectories under the influence of the PPM focusing field shown in Fig 1(a) and the self-electric and self-magnetic forces of the equilibrium beams. Shown in (a) is for Case I with single particle canonical angular momentum $\hat{P}_\theta = 0$, and in (b) for Case II with single particle canonical angular momentum $\hat{P}_\theta / 4\varepsilon = -0.99$.

To summarize the results of this section briefly, we find from self-consistent simulations and detailed phase space analysis that in the absence of RF signal, the equilibrium beam transport in the PPM focusing klystron is robust and no beam loss is expected. These results are in good agreement with the experimental observation [10] of 99.9% beam transmission in the absence of RF signal.

IV. HALOS INDUCED BY MISMATCHED ENVELOPE OSCILLATIONS

Microwave generation in a klystron is due to the coupling of large-amplitude charge-density and current oscillations in the electron beam with the output RF cavity. The charge-density and current oscillations result from the beating of the fast- and slow-space-charge waves on the electron beam, and are primarily longitudinal. From the point of view of beam transport, the charge-density and current oscillations perturb the equilibrium beam envelope discussed in Sec. III. Although a quantitative understanding of the effects of such large-amplitude charge-density and current oscillations on the dynamics of the electron beam is not available at present, especially in the transverse direction, a qualitative study of such effects is presented in this section. In the present analysis, use is made of the standard one-dimensional cold-fluid model to estimate the amplitude of the envelope mismatch induced by longitudinal current oscillations, and the two-dimensional electrostatic model described in Sec. II is used to explore the process of electron beam halo formation in the transverse phase space of the electron beam.

A. Estimation of the Mismatch Amplitude

It follows from the linearized continuity equation that the current perturbation $(\delta I_b)_{f,s}$ is related to the axial velocity perturbation $c(\delta \beta_b)_{f,s}$ by [18,19]

$$\frac{(\delta I_b)_{f,s}}{I_b} \cong -\frac{\omega}{\omega - \beta_b c k_{f,s}} \frac{(\delta \beta_b)_{f,s}}{\beta_b}, \tag{9}$$

where subscripts f and s denotes the fast- and slow-space-charge waves, respectively, and ω and $k_{f,s}$ are the frequency and wave numbers of the perturbations, respectively. Making the long-wavelength approximation for a thin beam, it can be shown that the dispersion relations for the fast- and slow-space-charge waves can be expressed as [18]

$$\omega - \beta_b c k_{f,s} = \pm \frac{\sqrt{\varepsilon_{sc}}}{\gamma_b \beta_b^2} \omega, \tag{10}$$

where k_f assumes plus sign, and k_s assumes minus sign. In Eq. (10), ε_{sc} is the longitudinal space-charge coupling parameter. The effective value of ε_{sc} is estimated to be $\varepsilon_{sc} = 0.012$ for the SLAC PPM focusing klystron [10]. In the klystron, the total current oscillations are the sum of fast- and slow-space-charge waves with a phase difference of $\sim 180°$. As a result, the total

current oscillations and the total velocity oscillations are out of phase by $\sim 180°$. Therefore, the amplitude of the total current oscillations is given by

$$\frac{\left(\delta I_b\right)_{total}}{I_n} \cong -\frac{2\gamma_b\beta_b^2}{\sqrt{\varepsilon_{sc}}}\frac{\left(\delta\beta_b\right)_{total}}{\beta_b}. \tag{11}$$

This has the important consequence that the perveance of the electron beam varies dramatically along the beam. From the definition of the perveance in Eq. (1), it is readily shown that the amplitude of perveance variation is given by

$$\frac{\delta K}{K} \cong \left(1+\frac{3\gamma_b\sqrt{\varepsilon_{sc}}}{2\beta_b^2}\right)\frac{\left(\delta I_b\right)_{total}}{I_b}. \tag{12}$$

For the SLAC PPM focusing klystron [10], Eq. (12) yields $\delta K / K = 1.45 \times \left(\delta I_b\right)_{total} / I_b$. At the RF output section, $\delta K / K$ exceeds unity considerably because $\delta I_b / I_b \approx 1$. (Note that the current oscillations in the RF output section are highly nonlinear and the maximum current exceeds $2I_b$.) From the beam envelope equation (8), the relative amplitude of beam envelope mismatch is estimated to be $\delta r_b / r_b = 0.56$, where r_b is the equilibrium beam radius and $\delta I_b / I_b = 1$ is assumed. In the self-consistent simulations presented below, we use $\delta r_b / r_b = 1.0$ in order to take into account the fact that the instantaneous current exceeds $2I_b$ during high-power operation of the klystron.

B. Self-Consistent Simulation of Electron Beam Halo Formation

The process of halo formation in intense electron beams is studied using the two-dimensional self-consistent model described in Sec. II. Results of the simulations are summarized in Figs. 5-10 for Cases I and II. In the simulations, 4096 macroparticles are used, and the macroparticles are loaded according to the rigid-rotor Vlasov distribution [15] with an initial beam radius of $2r_b(0)$, where $r_b(0)$ is the equilibrium beam radius at $s = 0$ [see Figs. 1(b) and 1(c) for Cases I and II, respectively]. The effect of current oscillation build up in the PPM focusing klystron, which requires three-dimensional modeling, is not included in the present two-dimensional simulation.

We first discuss the results of the self-consistent simulation for Case I. In Fig. 5, the effective beam core radius is plotted as a function of the propagation distance s. The solid curve is obtained from the self-consistent simulation, and the dotted curve is obtained by numerically solving the envelope equation (8) with the emittance calculated in the self-consistent simulation. As expected, results from the self-consistent simulation and envelope equation are in excellent agreement. Although the core radius oscillations are not exactly periodic due to emittance growth, the core radius oscillates with an approximate period of 11.5 cm, such that the envelope typically executes four periods of oscillations in the entire PPM focusing section of the SLAC PPM focusing klystron which is 42 cm long.
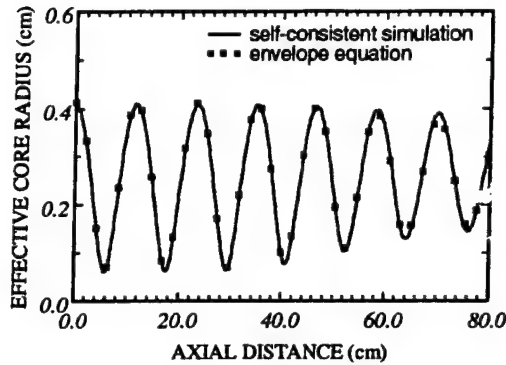
Figure 5. Plot of the effective beam core radius $r_b(s)$ versus the propagation distance s for mismatched beam propagation corresponding to Case I. The solid curve is obtained from the self-consistent simulation, whereas the dotted curve is obtained by numerically solving the envelope equation (8) with the emittance calculated in the self-consistent simulation.

Figure 6 shows the phase-space distributions of the electrons at several axial distances during the fourth period of the beam core radius oscillation for Case I. In contrast to the equilibrium phase-space distribution (Fig. 3), significant halos appear at $s = 34.7$, 37.8, 42.0, 44.1, and 46.2 cm. In the configuration space plots shown in Figs. 6(a) to 6(e) we observe a large variation in the beam core radius during the mismatched envelope oscillation period. The halo particles reach a maximum radius of $r_h = 6.4$ mm at $s = 42.0$ cm, where the beam core radius is a minimum and the traveling-wave RF output section is located. Around 1.5% of the electrons are found in the halo at that axial position. Because the maximum halo radius of $r_h = 6.4$ mm is greater than the actual beam tunnel radius $r_T = 4.7625$ mm, these halo electrons are lost to the waveguide wall. Therefore, the simulation results show that there will be 1.5% beam electron loss. In terms of beam power loss, 1.5% beam electron loss in the simulation corresponds to 0.2% beam power loss because the lost electrons have given up 88% of their kinetic energies (or have slowed down by about a factor of 2 in their axial velocities). The simulation results agree qualitatively with 0.8% beam power loss observed in the experiment [10]. The discrepancy between the simulation and experimental measurements may be caused by nonlinearities in the applied magnetic fields which are not included the present simulation as well as by three-dimensional effects which are not included in the two-dimensional simulation. It will be shown in Section V that three-dimensional effects do have a strong influence on the confinement of highly bunched beams.

As the beam propagates in the focusing field, its distribution rotates clockwise in the $(x, dx/ds)$ phase space, as shown in Figs. 6(f) to 6(j). The particles are initially dragged into the halo at the edges of the phase space distribution, where a chaotic region is formed around an unstable periodic orbit that is located just outside the beam distribution [20]. The unstable periodic orbit is a result of a resonance between the mismatched core envelope oscillations and the particles dynamics. As the halo particles move away from the beam core, the influence of
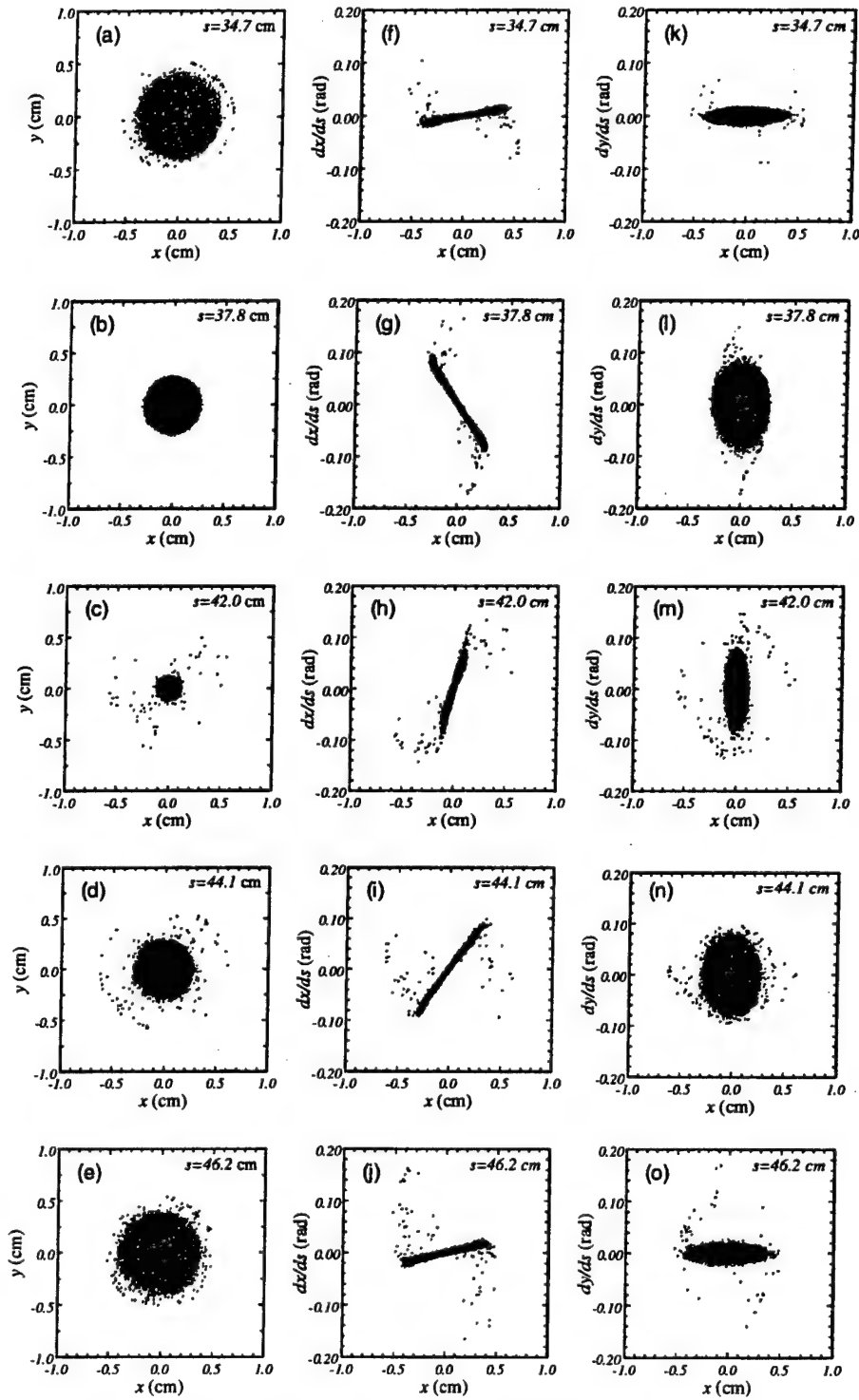
Figure 6. Plots of particle distributions in phase space at $s = 34.7$, 37.8, 42.0, 44.1, and 46.2 cm for Case I.
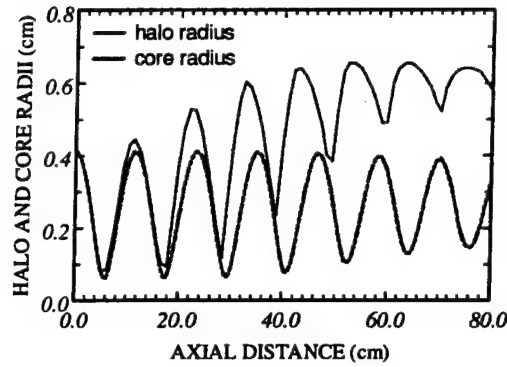
Figure 7. Plots of the halo radius (solid curve) and core radius (dashed curve) as a function of the propagation distance s for Case I.

space charge forces decreases and these halo particles start rotating faster than the core particles, creating the S-shaped distributions observed in Figs. 6(f) to 6(j).

The halo formation is also observed in the $(x, dy/ds)$ phase space distributions shown in Figs. 6(k) to 6(o). Although the macroscopic (average) canonical angular momentum $\langle \hat{P}_\theta \rangle$ is constant in the simulation, the distributions presented in Figs. 6(k) to 6(o) indicate that the distribution of single particle canonical angular momenta induces spread in the $(x, dy/ds)$ phase space.

Shown in Fig. 7 are the halo radius, i.e., the maximum radius achieved by all of the macroparticles in the self-consistent simulation, and the effective beam core radius as a function of the propagation distance for Case I. It is apparent in Fig. 7 that the halo formation process takes place essentially during the first 4 periods of the envelope oscillations. After reaching $r_h = 6.4$
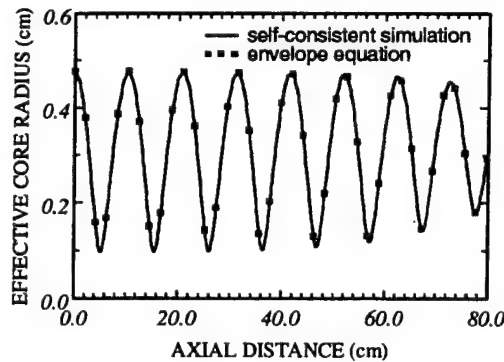

Figure 8. Plot of the effective beam core radius $r_b(s)$ versus the propagation distance s for mismatched beam propagation corresponding to Case II. The solid curve is obtained from the self-consistent simulation, whereas the dotted curve is obtained by numerically solving the envelope equation (8) with the emittance calculated in the self-consistent simulation.
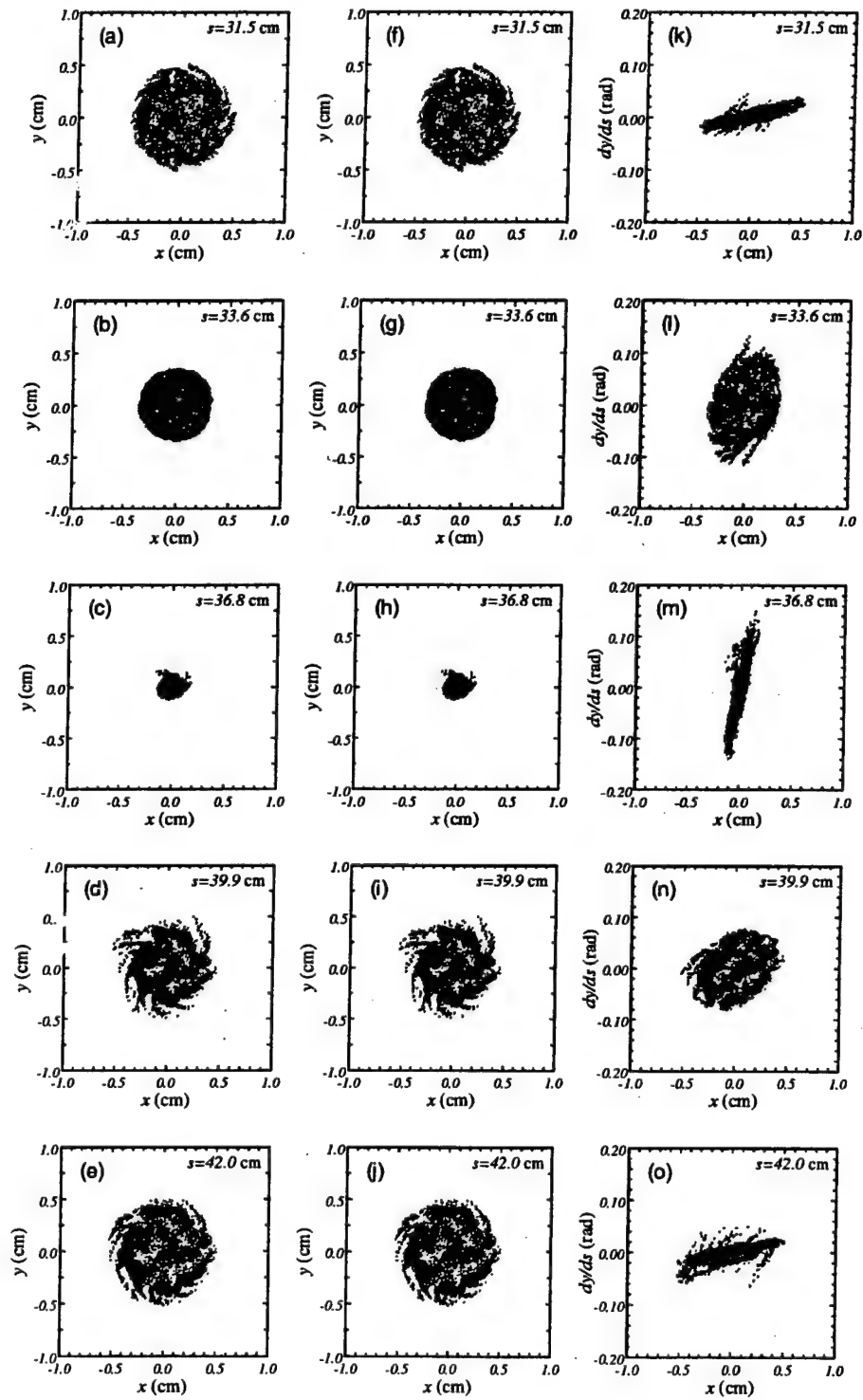
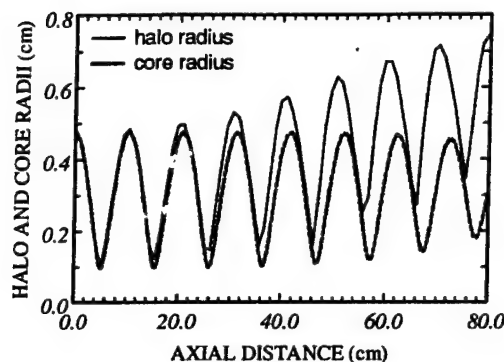Figure 9. Plots of particle distributions in phase space at $s = 31.5$, 33.6, 36.8, 39.9, and 42.0 cm for Case II.

Figure 10. Plots of the halo radius (solid curve) and core radius (dashed curve) as a function of the propagation distance s for Case II.

at $s = 42.0$ cm, the halo radius saturates. It is interesting to note that once the halo is developed, the halo radius and core envelope radius oscillate in opposite phase, with the former being maximum when the latter is minimum [as seen in Fig. 6(c)] and vice versa.

Second, we discuss the self-consistent simulation results for Case II and the role of small residual magnetic field at the cathode in the halo formation process. Figure 8 shows a plot of the effective beam core radius as a function of the propagation distance s. In Fig. 8, an excellent agreement is found between the envelope obtained from the self-consistent simulation (solid curve) and the envelope obtained by numerically solving the envelope equation (8) with the emittance calculated in the self-consistent simulation (dotted curve). One of the effects of the residual magnetic field at the cathode is to decrease the period of the envelope oscillations. The period for case II is 10.5 cm, slightly shorter than the period found in Case I (Fig. 5). The envelope executes four periods of oscillations in the entire PPM focusing section of the SLAC klystron.

Figure 9 shows the phase-space distributions of the electrons at several axial distances during the fourth period of the beam core radius oscillations for Case II. The configuration space distributions shown in Figs. 9(a) to 9(e) do not exhibit sizable halos. In particular, comparing Figs. 9(a)-9(e) with the configuration space distributions for Case I, shown in Figs. 6(a)-6(e), it is clear that the halos are much more pronounced in Case I. Analyzing Figs. 9(d) and 9(e) in more detail we observe hollow regions in the interior of the beam and that the existing halos appear in the form of vortices. Because the beam rotation period is calculated to be approximately 3 times the envelope oscillation period, the hollow regions and associated vortex structure might be a result of a diocotron instability process driven by a resonance between the envelope oscillations and the beam rotation.

The properties of the phase space distributions shown in Figs. 9(f) to 9(o) resemble the properties discussed in Case I with regard to the rotation in the $(x, dx/ds)$ phase space and the spread in the $(x, dy/ds)$ phase space. In comparison with Case I, the main difference is that the phase space distributions in Case II exhibit vortex structures.

Figure 10 shows the halo radius and effective beam core radius as a function of the propagation distance for Case II. Although sizable halos arise in the simulation after many periods of envelope oscillations, it is evident that the halo formation process is slower in Case II than in Case I (see Fig. 7). In particular, despite that the initial beam radius in Case II is larger than in Case I, the halo radius in Case I is greater than that in Case II at the output section ($s = 42$ cm) of the PPM focusing klystron. Because the halo radius at $s = 40$ cm is 5.3 mm and is still greater than the beam tunnel radius, the electrons in the halo are lost to the waveguide wall. Nevertheless, these results indicate that a small residual magnetic field at the cathode plays an important role in delaying the halo formation process and might be used to prevent electron beam loss in future experiments.

V. CONFINEMENT CRITERION FOR BUNCHED BEAMS

In this section, we study the confinement of a highly bunched beam propagating through a perfectly conducting drift tube in a uniform magnetic field. In the present analysis, a highly bunched beam is treated as a periodic array of point charges, while a unbunched beam is considered as a line charge, as illustrated in Fig. 11, where a is the radius of the drift tube and L is the period. In Fig. 11, the point charge represents a bunch in a highly bunched beam. Use is made of eigenfunction expansion to compute the Green's functions for the Poisson equation for both the line charge and the periodic array of point charges [14]. Making use of these Green's functions, we compute the electrostatic potential due to the surface charge on the perfectly conducting drift tube. With a proper choice of the vector potential for the applied uniform magnetic field $B_0 \hat{e}_z$, we derive and analyze non-relativistic Hamilton's equations of motion for both the line charge and the periodic array of point charges.
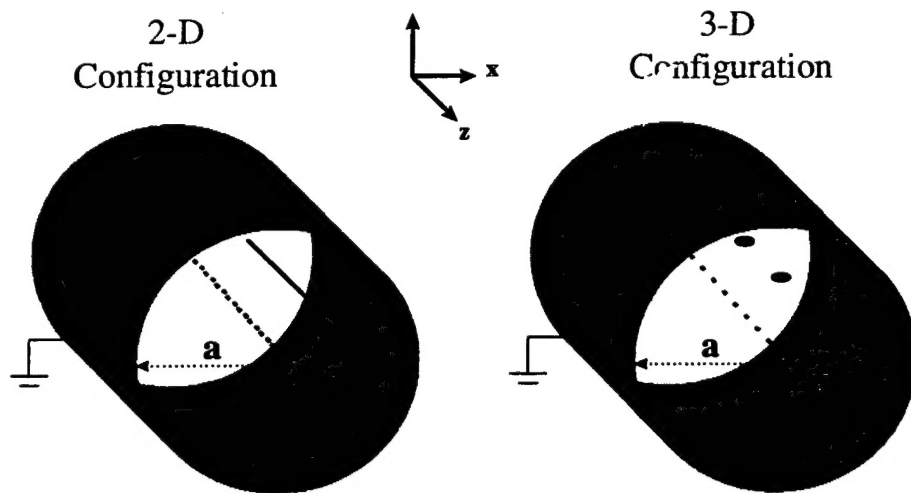

Figure 11.   Schematics of a line charge and a periodic array of point charges in a perfectly conducting drift tube.
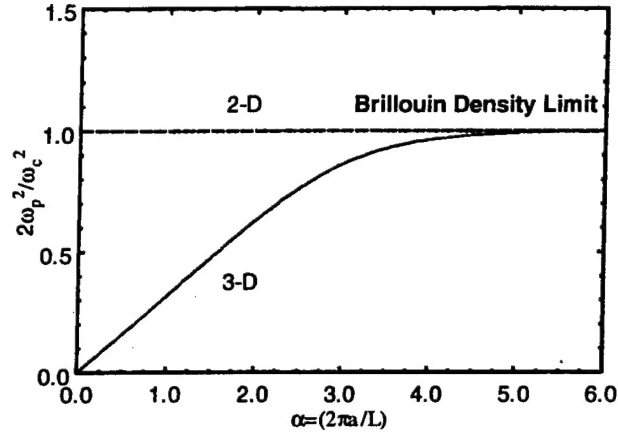
Figure 12. Plot of the highest value of the effective self-field parameter $2\omega_p^2 / \omega_c^2$ as a function of $\alpha = 2\pi a / L$ for radial confinement of unbunched (2D) and highly bunched (3D) beams.

It can be shown [21] that for a charge bunch with canonical angular momentum $P_\theta = 0$, the condition for radial confinement is given by

$$\frac{2\omega_p^2}{\omega_c^2} < \frac{1}{1 + \sum_{n=1}^{\infty} \frac{n\alpha}{I_0(n\alpha)I_1(n\alpha)}}, \tag{13}$$

where $\alpha = 2\pi a / L$, $I_0(x)$ and $I_1(x)$ are the zeroth- and first-order modified Bessel functions of the first-kind, respectively, $\omega_p^2 = (4\pi e^2 / m)(N_{bunch} / \pi a^2 L)$ is the effective plasma frequency squared with N_{bunch} being the number of electrons per bunch, and $\omega_c = eB_0 / mc$ is the nonrelativistic electron cyclotron frequency. Figure 12 shows the highest value of the effective self-field parameter $2\omega_p^2 / \omega_c^2$ as a function of $\alpha = 2\pi a / L$ for radial confinement. Note that the well-known Brillouin density limit with $2\omega_p^2 / \omega_c^2 = 1$ [22] is recovered by taking $L \rightarrow 0$ while holding the effective plasma frequency ω_p fixed.

The results shown in Fig. 12 suggest that a stronger magnetic field is required to confine a beam as it becomes bunched in the axial direction. Work is in progress to examine the full effect of bunching on halo production in high-power PPM klystron amplifiers.

VI. CONCLUSIONS

We have studied the behavior of a high-intense electron beam under a current-oscillation-induced mismatch between the beam and the magnetic focusing field, using a two-dimensional

self-consistent electrostatic model. For high-intensity electron beams, it was found from the simulations that sizable halos appear after the beam envelope undergoes several mismatched oscillations, depending on the amplitude of mismatched beam envelope oscillations. Detailed simulation results were presented for the choice of system parameters corresponding to the 50 MW, 11.4 GHz periodic permanent magnetic (PPM) focusing klystron experiment at the Stanford Linear Accelerator Center (SLAC). The simulation results were in qualitative agreement with the experimental observation of 1% beam power loss in the SLAC PPM focusing klystron.

We have also derived a criterion for the confinement of a highly bunched beam propagating through a perfectly conducting drift tube in a uniform magnetic field. This confinement criterion suggests that a stronger magnetic field is required to confine a beam as it becomes bunched in the axial direction. Work is in progress to examine the full effect of bunching on halo production in high-power PPM klystron amplifiers.

ACKNOWLEDGMENTS

REFERENCES

1. See, for example, *Special Issue on High-Power Microwave Generation*, edited by E. Schamiloglu and Y. Y. Lau, IEEE Trans. Plasma Sci., vol. 26, No. 3, June, 1998.
2. F. J. Agee, "Evolution of pulse shortening research in narrow band, high-power microwave sources," IEEE Trans. Plasma Sci., vol. 26, No. 3, pp. 235-245, 1998.
3. J. Benford and G. Benford, "Pulse shortening in high-power microwave sources," Proceedings of the 11th International Conference on High-Power Particle Beams, Institute of Plasma Physics, Academy of Science of the Czech Republic, 1996, p. 217.
4. K. J. Hendricks, P. D. Coleman, R. W. Lemke, M. J. Arman, and L. Bowers, "Extraction of 1 GW of rf power from an injection locked relativistic klystron oscillator," Phys. Rev. Lett., vol. 76, No. 1, pp. 154-157, Jan., 1996; and references therein.
5. M. D. Haworth, G. Baca, J. N. Benford, T. Englert, K. Hackett, K. J. Hendricks, D. Henley, M. LaCour, R. W. Lemke, D. Price, D. Ralph, M. Sena, D. Shiffler, and T. A. Spencer, "Significant pulse-lengthening in a multigigawatt magnetically insulated transmission line oscillator," IEEE Trans. Plasma Sci., vol. 26, No. 3, pp. 312-319, 1998.
6. F. Hegeler, C. Grabowski, and E. Schamiloglu, "Electron density measurements during microwave generation in a high-power backward-wave oscillator," IEEE Trans. Plasma Sci., vol. 26, No. 3, pp. 275-281, June, 1998.
7. D. Price, J. S. Levine, and J. N. Benford, "Diode plasma effects on the microwave pulse length from relativistic magnetrons," in *Intense Microwave Pulses V*, edited by H. E. Brandt, Proc. SPIE, vol. 3158, 1997, p. 13.
8. C. Chen and R. A. Jameson, "Self-consistent simulation studies of periodically focused intense charged-particle beams," Phys. Rev. E, vol. 52, No. 3, pp. 3074-3080, Sept., 1995.

9. Y. Fink, C. Chen, and W. P. Marable, "Halo formation and chaos in root-mean-square matched beams propagating through a periodic solenoidal focusing channel," Phys. Rev. E, vol. 55, No. 6, pp. 7557-7564, June, 1997.

10. D. Sprehn, G. Caryotakis, E. Jongewaard, and R. M. Phillips, "Periodic permanent magnetic development for linear collider X-band klystrons," Proc. XIX International Linac Conf., Argonne National Laboratory Report ANL-98/28, 1998, p. 689.

11. C. Chen and R. Pakter, "Halo formation in intense electron beams in high-power klystron amplifiers," in *Intense Microwave Pulses VI*, edited by H. E. Brandt, SPIE Proc. vol. 3702, 1999, p. 21.

12. C. Chen and R. Pakter, "Mechanisms and control of beam halo formation in intense microwave sources and accelerators," Phys. Plasmas, vol. 7, 2000, in press.

13. R. Pakter and C. Chen, "Electron beam halo formation in high-power periodic permanent magnetic focusing klystron amplifiers," IEEE Trans. Plasma Sci., vol. 29, 2000, in press.

14. M. Hess, R. Pakter, and C. Chen, "Green's function description of space charge in intense charged-particle beams," Proceedings of 1999 Particle Accelerator Conference, 1999, p. 2752.

15. C. Chen, R. Pakter, and R. C. Davidson, "Rigid-rotor Vlasov Equilibrium for an intense charged-particle beam propagating through a periodic solenoidal magnetic field," Phys. Rev. Lett., vol. 79, No. 2, pp. 225-228, July, 1997.

16. R. C. Davidson and C. Chen, "Kinetic description of high-intensity beam propagation through a periodic focusing field based on the nonlinear Vlasov-Maxwell equations," Part. Accel., vol. 59, pp. 175-250, 1998.

17. C. Chen, R. Pakter, and R. C. Davidson, "Phase space structure for matched intense charged-particle beams in periodic focusing transport systems," Phys. Plasmas, vol. 6, No. 9, pp. 3674-3657, 1999.

18. C. Chen, G. Bekefi, and P. Catravas, "Growth and saturation of simulated beam modulation in a two-stream relativistic klystron amplifier," Appl. Phys. Lett., vol. 62, No. 14, pp. 1579-1581, April 1993.

19. M. Friedman, J. Krall, Y. Y. Lau, and V. Serlin, "Efficient generation of multigigawatt rf power by a klystronlike amplifier," Rev. Sci. Instrum., vol. 61, No. 1, pp. 171-181, Jan., 1990.

20. R. L. Gluckstern, "Analytic model for halo formation in high-current ion linacs," Phys. Rev. Lett., vol. 72, No. 9, pp. 1247-1250, August, 1994.

21. M. Hess and C. Chen, "Criterion for confinement of intense bunched beams," manuscript in preparation, 2000.

22. R. C. Davidson, *Physics of Nonneutral Plasmas,* Addison-Wesley, Reading, MA, 1990, p. 46.